CERN–2016–xxx
31 January 2016

Draft version o.0

ORGANISATION EUROPÉENNE POUR LA RECHERCHE NUCLÉAIRE

CERN **EUROPEAN ORGANIZATION FOR NUCLEAR RESEARCH**

Handbook of LHC Higgs cross sections:
4. Deciphering the nature of the Higgs sector

Report of the LHC Higgs Cross Section Working Group

Editors: C. Anastasiou
D. de Florian
C. Grojean
F. Maltoni
C. Mariotti
A. Nikitenko
M. Schumacher
R. Tanaka

GENEVA
2016

Contents

---

[1] B. Mellado, P. Musella, M. Grazzini, R. Harlander (eds.); plus Authors

[2] F. Caola, Y. Gao, N. Kauer, L. Soffi, J. Wang (eds.); N. Fidanza, N. Greiner, A. Gritsan, G. Heinrich, S. Höche, F. Krauss, Y. Li, S. Liebler, C. O'Brien, S. Pozzorini, U. Sarica, M. Schulze, F. Siegert, G. Weiglein, A. Contributor, . . .

Part I

Standard Model Predictions[1]

[1] B. Mellado, P. Musella, M. Grazzini, R. Harlander (eds.); plus Authors

Chapter 1

Off-shell Higgs production and Higgs interference [1]

1 Introduction

Introduction/overview

2 Input parameters and PDF recommendation for the $gg\ (\to H) \to VV$ interference

Adopting LHCHXSWG-INT-2015-006 with G_μ scheme: $M_{\mathrm{W}} = 80.35797$ GeV, $M_Z = 91.15348$ GeV, $\Gamma_W = 2.08430$ GeV, $\Gamma_Z = 2.49427$ GeV, $M_t = 172.5$ GeV, $M_b(M_b) = 4.18$ GeV, $G_F = 1.1663787 \cdot 10^{-5}$ GeV^{-2} are used. $V_{CKM} = \mathbf{1}$. Finite top and bottom quark mass effects are included. Lepton and light quark masses are neglected. pp collisions at $\sqrt{s} = 13$ TeV. Use NLO PDF set `PDF4LHC15_nlo_100` (NF=5) throughout (arXiv:1510.03865). PDF set used with α_s obtained in same fit.

QCD scale: $\boldsymbol{\mu_R = \mu_F = M_{VV}/2}$. A fixed-width Breit-Wigner propagator $D(p) \sim (p^2 - M^2 + iM\Gamma)^{-1}$ is employed for W, Z and Higgs bosons ($M, \Gamma \leftrightarrow$ complex pole). The SM Higgs mass is set to 125 GeV. The SM Higgs width parameter is calculated using the HDECAY code v6.50 (hep-ph/9704448). For $M_H = 125$ GeVone obtains $\Gamma_H = 4.097 \cdot 10^{-3}$ GeV.

Remark: In agreement with HDECAY, the W and Z masses and widths have been changed from physical on-shell masses to the pole values, see eq. (7) in LHCHXSWG-INT-2015-006. The relative deviation is at the $3 \cdot 10^{-4}$ level.

PDF set order recommendation for gg $(\to H) \to$ VV signal-background interference: use a NLO PDF set

Justification:

Combining any n-order PDF fit with a m-order parton-level calculation is theoretically consistent as long as $n \geq m$. Deviations are expected to be of higher order if same α_s is used.

The problem with the LO gluon PDF: especially in the Higgs region, it is mostly determined by DIS data. At LO, DIS does not have a gluon channel, which enters at NLO (with a large K-factor). A LO fit cannot take this into account, so it has to fit something where about half of the prediction is missing. In the fit, there is some freedom in the gluon, which is only determined by the evolution, so it adjusts in order to compensate for a large missing contribution in the LO cross section.

3 $H \to ZZ$ and $H \to WW$ modes

3.1 TBD

Squared amplitude comparison

Compare $\overline{\Sigma}|\mathcal{M}|^2$ in GeV^n, where $g_s = 1$ is imposed for one phase space point to validate programs/tools against each other at differential level.

Squared amplitude: 1) signal: $\overline{\Sigma}\left|\mathcal{M}_{signal}\right|^2$, 2) interference: $\overline{\Sigma}\, 2\,\mathrm{Re}(\mathcal{M}^*_{signal}\, \mathcal{M}_{background})$

Clarification: $\mathcal{M}_{signal}$ contains all graphs with Higgs propagator (s- and t-channel), $\mathcal{M}_{background}$ contains all graphs with no Higgs propagator (connecting the same initial and final state as $\mathcal{M}_{signal}$ at the corresponding order; all non-vanishing intermediate states/graphs are to be taken into account even if they are negligible for phenomenological cross

[1] F. Caola, Y. Gao, N. Kauer, L. Soffi, J. Wang (eds.); N. Fidanza, N. Greiner, A. Gritsan, G. Heinrich, S. Höche, F. Krauss, Y. Li, S. Liebler, C. O'Brien, S. Pozzorini, U. Sarica, M. Schulze, F. Siegert, G. Weiglein, A. Contributor, …

section calculations)
(Normalisation validation via benchmark off-peak cross sections with minimal cuts, see below.)

GGF phase space point: $p_1\, p_2 \;\to\; p_3\, p_4\, p_5\, p_6$ (in/out), $p_i^2 = 0$ for $i = 1, \ldots, 6$

PS_GGF	E [GeV]	p_x [GeV]	p_y [GeV]	p_z [GeV]
p_1	4.362170681118732	0.000000000000000	0.000000000000000	4.362170681118732
p_2	902.6536183436683	0.000000000000000	0.000000000000000	–902.6536183436683
p_3	235.0932249209668	31.07371048696601	–8.904984169817602	–232.8603662653819
p_4	442.9175507598575	–50.03334210777508	–17.50581180266772	–439.7342015374366
p_5	19.64404884528074	5.501965298945947	6.434523012322202	–17.72608096813466
p_6	209.3609644986807	13.45766632186332	19.97627296016339	–207.970798891595

Particle mapping to $p_1 p_2 \to p_3\; p_4\; p_5\; p_6$:
2l2l, 4l, 2l2ν (fully leptonic processes): $gg \to e^+ e^-\; \overline{X}\; X$ ($X = \mathrm{e}, \mu, \nu$), $gg \to e^+ \nu_e \bar{\nu}_\mu \mu^-$
(distinguish diff. flavour and same flavour cases where applicable)

$l\bar{\nu}jj$, $l\bar{l}jj$ (semileptonic processes, light quark flavour type 1, e.g. $q_{1u} = u$, $q_{1d} = d$):
$gg \to \bar{\nu}_\ell \ell \bar{q}_{1d} q_{1u},\; gg \to \bar{\ell} \nu_\ell \bar{q}_{1u} q_{1d},\; gg \to \bar{\ell}\ell \bar{q}_{1u} q_{1u},\; gg \to \bar{\ell}\ell \bar{q}_{1d} q_{1d}$

VBF phase space point: $p_1\, p_2 \;\to\; p_3\, p_4\, p_5\, p_6\, p_7\, p_8$ (in/out), $p_i^2 = 0$ for $i = 1, \ldots, 8$

PS_VBF	E [GeV]	p_x [GeV]	p_y [GeV]	p_z [GeV]
p_1	1291.9388816019043	0.0000000000000000	0.0000000000000000	1291.9388816019043
p_2	559.29955902360803	0.0000000000000000	0.0000000000000000	-559.29955902360803
p_3	96.157113352629182	-59.808617976628611	-41.531770786050167	-62.803118389225403
p_4	79.923048731952122	-56.889731449070219	-51.341666707035863	22.699899427229077
p_5	74.789443907018224	-23.846942654447435	-13.621303489630101	-69.564677367180494
p_6	84.482934407387020	-1.5542559324534224	61.101450118849762	-58.322922491530264
p_7	301.73807933052944	-31.037247532417634	-26.779908707068554	-298.94045272148998
p_8	1214.1478208959963	173.13679554501735	72.173199570934926	1199.5705941204933

Particle mapping to $p_1 p_2 \to p_3\; p_4\; p_5\; p_6\; p_7\; p_8$:
$p_3\; p_4\; p_5\; p_6$ as for GGF; subset: $p_1\; p_2\; p_7\; p_8 = \bar{q}_{1u} q_{2u}\; \overline{X}_1\; X_2$ ($X \in \{q_u, q_d\}$ with light quark flavour types 1 and 2, e.g. $q_{1u} = u$, $q_{1d} = d$, $q_{2u} = c$, $q_{2d} = s$)

Off-shell and interference key/benchmark cross sections and distributions for gluon fusion (rescaled LO) and VBF (LO and NLO)

SM Higgs cross sections: 1) signal, 2) signal+full interference, 3) full interfering gg continuum background only
final states ($\mathrm{l} = \mathrm{e}, \mu$, $\nu = \nu_\mathrm{e}, \nu_\mu, \nu_\tau$): 2l2l (diff. flavour), 4l (same flavour), 2l2ν (diff. flavour and same flavour: $\mathrm{l}\bar{\mathrm{l}}'$ $[WW]$; $\mathrm{l}\bar{\mathrm{l}}$ $[ZZ\&WW]$, for $\overline{\Sigma}|\mathcal{M}|^2$ comparison: $\mathrm{l}\bar{\mathrm{l}}\nu'\bar{\nu}'$, $\mathrm{l}\bar{\mathrm{l}}\nu_\mathrm{l}\bar{\nu}_\mathrm{l}$), $\mathrm{l}\bar{\nu}jj$, $\mathrm{l}\bar{\mathrm{l}}jj$ (subprocesses see above):
Regions definded via M_{VV} or M_T cuts (cross sections calculated with minimal cuts, cut set 1, see below):
off-peak: $M_{VV} > 140$ GeV
far off-peak I: $220 < M_{VV} < 300$ GeV(interference)
far off-peak II: $M_{VV} > 300$ GeV(signal enriched)
on-peak (4l and WW channels only): M_{VV} in 110–140 GeV
For $WW \to$ 2l2ν channel also:
far off-peak M_T I: $M_{T,WW} > 200$ GeV
far off-peak M_T II: $M_{T,WW} > 350$ GeV
on-peak M_T: $M_{T,WW}$ in 60–140 GeV

Two selection cut sets for GGF:
1) **minimal cuts** ($M_{\mathrm{l}\bar{\mathrm{l}}}, M_{q\bar{q}} > 10$ GeV for all same-flavour $\mathrm{l}\bar{\mathrm{l}}$ and $q\bar{q}$ pairs, $p_{Tj} > 25$ GeV)
N.B. No cuts are applied for the 2l2ν final state with different charged lepton flavours.
2) **ATLAS and CMS Higgs off-shell search selections** (minimal cuts and below)

ATLAS and CMS Higgs off-shell search selections

Jets:
ATLAS: $p_{Tj} > 25$ GeV for $|\eta_j| < 2.4$, $p_{Tj} > 30$ GeV for $2.4 < |\eta_j| < 4.5$

CMS: $p_{Tj} > 30$ GeV for $|\eta_j| < 4.7$

H → ZZ → 4l channel:
ATLAS:
$p_{T\mathrm{l},1} > 20$ GeV
$p_{T\mathrm{l},2} > 15$ GeV
$p_{T\mathrm{l},3} > 10$ GeV
$p_{T\mathrm{e},4} > 7$ GeV
$p_{T\mu,4} > 6$ GeV
$|\eta_\mathrm{e}| < 2.47$
$|\eta_\mu| < 2.7$
$M_{4\mathrm{l}} > 220$ GeV

CMS:
$p_{T\mathrm{l},1} > 20$ GeV
$p_{T\mathrm{l},2} > 10$ GeV
$p_{T\mathrm{e},3,4} > 7$ GeV
$p_{T\mu,3,4} > 5$ GeV
$|\eta_\mathrm{e}| < 2.5$
$|\eta_\mu| < 2.4$
$M_{4\mathrm{l}} > 220$ GeV

H → ZZ → 2l2ν channel:
ATLAS transverse mass definition (recommended for $M_{\mathrm{VV}} > 2M_\mathrm{Z}$):

$$M_{T,ZZ} = \sqrt{(M_{T,\ell\ell} + M_{T,miss})^2 - (\mathbf{p}_{T,\ell\ell} + \mathbf{p}_{T,miss})^2}\ ,\ \text{where}\quad M_{T,X} = \sqrt{p_{T,X}^2 + M_Z^2} \tag{1.1}$$

ATLAS:
$p_{T\mathrm{l}} > 20$ GeV(electron, muon)
$|\eta_\mathrm{e}| < 2.47$
$|\eta_\mu| < 2.5$
$E_{T,miss} > 180$ GeV
$\Delta\phi_{\mathrm{ll}} < 1.4$
$M_{T,ZZ} > 380$ GeV

CMS:
$p_{T\mathrm{l}} > 20$ GeV(electron, muon)
$E_{T,miss} > 80$ GeV
$M_{T,ZZ}$ used by CMS: Eq. (1.1) with M_Z replaced by $M_{\ell\ell}$

H→ WW → 2l2ν channel
ATLAS transverse mass definition (recommended):

$$M_{T,WW} = \sqrt{(M_{T,\ell\ell} + p_{T,miss})^2 - (\mathbf{p}_{T,\ell\ell} + \mathbf{p}_{T,miss})^2}\ ,\ \text{where}\quad M_{T,\ell\ell} = \sqrt{p_{T,\ell\ell}^2 + M_{\ell\ell}^2} \tag{1.2}$$

ATLAS:
$p_{T\mathrm{l},1} > 22$ GeV
$p_{T\mathrm{l},2} > 10$ GeV
$|\eta_\mathrm{e}| < 2.47$
$|\eta_\mu| < 2.5$
$M_{\mathrm{ll}} > 10$ GeV
$p_{T,miss} > 20$ GeV
reference: http://arxiv.org/abs/1412.2641

GGF: We will reweight LO cross sections and distributions with (estimated) NLO QCD K-factors where possible (see recommendations for details on how K factors are estimated)

VBF selection cuts
Regions definded via M_{VV} or M_T cuts (identical to GGF):
off-peak: $M_{VV} > 140$ GeV

far off-peak I: $220 < M_{VV} < 300$ GeV(interference)
far off-peak II: $M_{VV} > 300$ GeV(signal enriched)
on-peak (4l and WW channels only): M_{VV} in 110–140 GeV
For $WW \to 2l2\nu$ channel also:
far off-peak M_T I: $M_{T,WW} > 200$ GeV
far off-peak M_T II: $M_{T,WW} > 350$ GeV
on-peak M_T: $M_{T,WW}$ in 60–140 GeV

VBF common cuts:
Jets: $p_{Tj} > 20$ GeV, $|\eta_j| < 5.0$, anti-k_T jet clustering with $R = 0.4$, $M_{jj} > 60$ GeV for all jet pairs
Leptons: $p_{T\mathrm{l}} > 20$ GeV, $|\eta_\mathrm{l}| < 2.5$, $M_{\mathrm{l}\bar{\mathrm{l}}} > 20$ GeV for all same-flavour $\mathrm{l}\bar{\mathrm{l}}$ combinations
(exception: for the *on-peak* and *on-peak M_T* regions: apply $M_{\mathrm{l}\bar{\mathrm{l}}} > 10$ GeV instead)
Neutrinos: $E_{T,miss} > 40$ GeV
N.B. off-shell $M_{\mathrm{l}\bar{\mathrm{l}}}$ cut differs from GGF

Two selection cut sets for VBF (tagging jets: j_1, j_2, ordered by decreasing $|\eta_j|$):

1) **Loose VBF cuts**
in addition to the VBF common cuts:
$M_{j_1 j_2} > 130$ GeV

2) **Tight VBF cuts**
in addition to the VBF common cuts:
$M_{j_1 j_2} > 600$ GeV
$\Delta y_{j_1 j_2} > 3.6$
$y_{j_1} y_{j_2} < 0$ (opposite hemispheres)

Differential distributions
M_{VV}, for $VV \to 2l2\nu$ channels also $M_{T,VV}$ distributions, in all cases: bin size 10 GeVin $[0, 1]$ TeV, bin size 50 GeV in $[1, 3]$ TeV

Beyond SM: Higgs singlet model (1HSM)

benchmark results for heavy Higgs interference in GGF&VBF

Suggested 1HSM benchmark points:
YR3, Sec. 13.3, p. 232. In basis (335) we propose the following four benchmark points:
1) $M_{h_2} = 400$ GeV $\sin\theta = 0.2$,
2) $M_{h_2} = 600$ GeV, $\sin\theta = 0.2$,
3) $M_{h_2} = 600$ GeV, $\sin\theta = 0.4$,
4) $M_{h_2} = 900$ GeV, $\sin\theta = 0.2$.
$M_{h_1} = 125$ GeV, $\mu_1 = \lambda_2 = \lambda_1 = 0$ for all points.
Remark: Point 3) is clearly not compatible with current limits, but there's a tension between remaining within limits and demonstrating dependence on the mixing angle, which is also important.
Point 1): $\Gamma_{h_1} = 4.34901 \times 10^{-3}$ GeV, $\Gamma_{h_2} = 1.52206$ GeV
Point 2): $\Gamma_{h_1} = 4.34901 \times 10^{-3}$ GeV, $\Gamma_{h_2} = 5.95419$ GeV
Point 3): $\Gamma_{h_1} = 3.80539 \times 10^{-3}$ GeV, $\Gamma_{h_2} = 22.5016$ GeV
Point 4): $\Gamma_{h_1} = 4.34901 \times 10^{-3}$ GeV, $\Gamma_{h_2} = 19.8529$ GeV
(The widths have been calculated using FEYNRULES.)

GGF: GG2VV_EWS, MG5_AMC

VBF: PHANTOM, VBFNLO

GG2VV_EWS results:

		h_1	h_2		
$\sin\alpha$	M [GeV]	125	400	600	900
0.2	Γ [GeV]	4.34901×10^{-3}	1.52206	5.95419	19.8529
0.4	Γ [GeV]	3.80539×10^{-3}		22.5016	

Table 1.1: Widths of the physical Higgs bosons h_1 and h_2 in the 1-Higgs-Singlet Extension of the SM with mixing angles $\sin\theta = 0.2$ and $\sin\theta = 0.4$ as well as $\mu_1 = \lambda_1 = \lambda_2 = 0$.

$gg \to h_2 \to ZZ \to \ell\bar{\ell}\ell'\bar{\ell}'$ σ [fb], pp, $\sqrt{s} = 13$ TeV min. cuts			interference			ratio		
$\sin\alpha$	M_{h2} [GeV]	$S(h_2)$	I_{h1}	I_{bkg}	I_{full}	R_{h1}	R_{bkg}	R_{full}
0.2	400	0.07412(6)	0.00682(6)	-0.00171(2)	0.00511(6)	1.092(2)	0.977(1)	1.069(2)
0.2	600	0.01710(2)	-0.00369(3)	0.00384(3)	0.00015(4)	0.784(2)	1.225(2)	1.009(3)
0.2	900	0.002219(2)	-0.003369(9)	0.003058(8)	-0.00031(2)	-0.518(4)	2.378(4)	0.860(6)
0.4	600	0.07065(6)	-0.01191(6)	0.01465(6)	-0.00274(9)	0.831(2)	1.207(2)	1.039(2)

Table 1.2: Cross sections for $gg\ (\to \{h_1, h_2\}) \to ZZ \to \ell\bar{\ell}\ell'\bar{\ell}'$ in pp collisions at $\sqrt{s} = 13$ TeV at loop-induced leading order in the 1-Higgs-Singlet Extension of the SM with $M_{h1} = 125$ GeV, $M_{h2} = 400, 600, 900$ GeV and mixing angle $\sin\theta = 0.2$ or 0.4 as indicated. Results for the heavy Higgs (h_2) signal (S) and its interference with the light Higgs (I_{h1}) and the continuum background (I_{bkg}) and the full interference (I_{full}) are given. The ratio $R_i = (S+I_i)/S$ illustrates the relative change of the heavy Higgs signal due to interference with the light Higgs and continuum background amplitude contributions. Minimal cuts are applied, $M(V) > 4$ GeV and $p_T(V) > 1$ GeV. Cross sections are given for a single lepton flavour combination. The integration error is displayed in brackets.

$gg \to h_2 \to ZZ \to \ell\bar{\ell}\ell'\bar{\ell}'$ σ [fb], LHC, $\sqrt{s} = 13$ TeV min. cuts						
$\sin\alpha$	M_{h2} [GeV]	$S(h_2)$	h_1	gg bkg.	S(h_2) + h_1 + I_{h1}	all
0.2	400	0.07412(6)	0.854(2)	21.18(7)	0.934(2)	21.86(7)
0.2	600	0.01710(2)	0.854(2)	21.18(7)	0.867(2)	21.80(7)
0.2	900	0.002219(2)	0.854(2)	21.18(7)	0.852(2)	21.79(7)
0.4	600	0.07065(6)	0.734(2)	21.18(7)	0.793(2)	21.77(7)

Table 1.3: Cross sections for $gg\ (\to \{h_1, h_2\}) \to ZZ \to \ell\bar{\ell}\ell'\bar{\ell}'$ in pp collisions at $\sqrt{s} = 13$ TeV at loop-induced leading order in the 1-Higgs-Singlet Extension of the SM with $M_{h1} = 125$ GeV, $M_{h2} = 400, 600, 900$ GeV and mixing angle $\sin\theta = 0.2$ or 0.4 as indicated. Results for the heavy Higgs (h_2) signal (S), light Higgs background (L) and continuum background (B). Where more than one contribution is indicated, all interferences are taken into account. The ratio $R_i = (S+i+I_i)/(S+i)$ illustrates the relative change of the indicated contributions including interference to the contributions with no interference. Other details are as in Table 1.2.

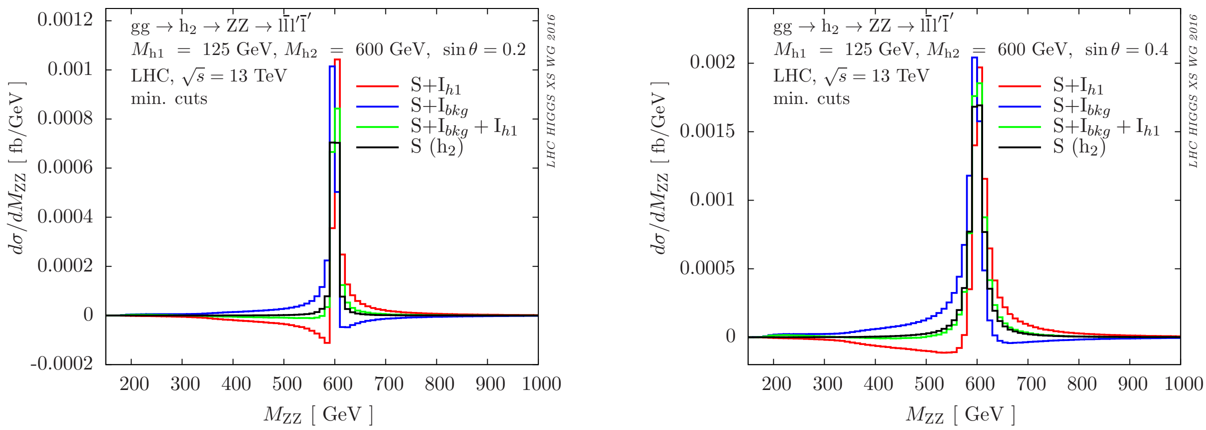

Fig. 1: Invariant mass distributions for $gg\ (\to \{h_1, h_2\}) \to ZZ \to \ell\bar{\ell}\ell'\bar{\ell}'$, other details as in Table 1.2.

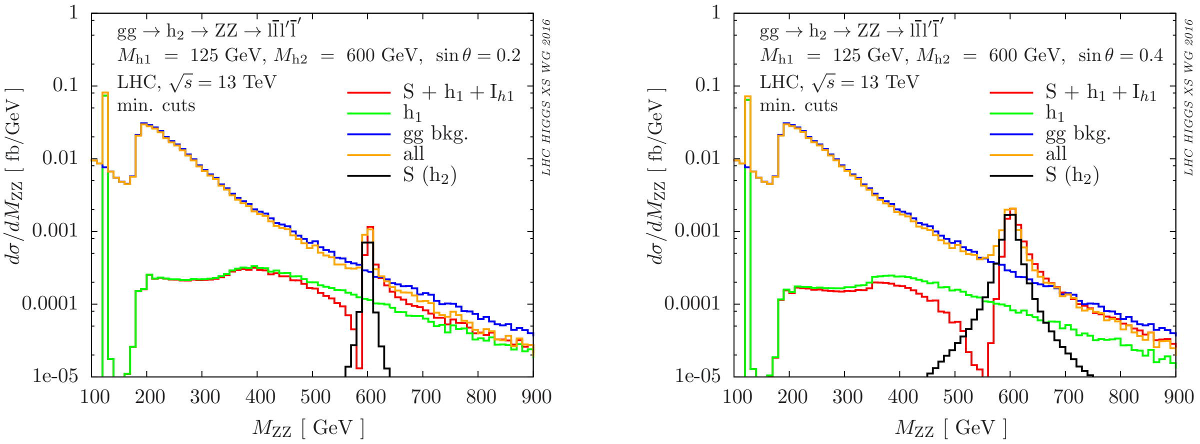

Fig. 2: Invariant mass distributions for gg $(\to \{h_1, h_2\}) \to ZZ \to \ell\bar{\ell}\ell'\bar{\ell}'$, other details as in Table 1.3. Where more than one contribution is included, all interferences are taken into account.

3.2 Multijet merging effects in $gg \to \ell\bar{\nu}_\ell\bar{\ell}'\nu_{\ell'}$ using SHERPA

3.2.1 Set-up

In this section, results for the loop–induced process $gg \to \ell\bar{\nu}_\ell\bar{\ell}'\nu_{\ell'}$ obtained with the SHERPA event generation framework [1] will be presented, with the goal to highlight the effect of multijet merging [2] on some critical observables. This is accomplished by directly comparing the results where the leading order processes depicted in Figure 3 have been supplemented with the parton shower (labelled LOOP2+PS) with a sample where an additional jet has been produced, *i.e.* the quark-loop induced processes $gg \to \ell\bar{\nu}_\ell\bar{\ell}'\nu_{\ell'}g$ and $qg \to \ell\bar{\nu}_\ell\bar{\ell}'\nu_{\ell'}q$ (labelled MEPS@LOOP2) as shown in Figure 4. In addition, these two samples are further subdivided into those including a Higgs boson of $m_H = 125$ GeV and those where the Higgs boson has been decoupled with $m_H \to \infty$. Here, the matrix elements are provided from the OPENLOOPS +COLLIER package [3, 4] are being used. For parton showering, the implementation of [5] is employed, with a starting scale

$$\mu_Q^2 = p^2_{\perp,\ell\bar{\nu}_\ell\bar{\ell}'\nu_{\ell'}} + m^2_{\ell\bar{\nu}_\ell\bar{\ell}'\nu_{\ell'}}\,. \tag{1.3}$$

A similar analysis, although for centre-of-mass energies of 8 TeV has already been presented in [6]. Here, in addition, the effect of including a Higgs boson with mass $m_H = 125$ GeV is investigated, which was not the case in the previous analysis. Results without the Higgs boson are obtained by effectively decoupling it, pushing its mass to very high values in the calculation, $m_H \to \infty$.

3.2.2 Results

In this investigation the following cuts have been applied:

$$\begin{array}{rclcrcl} p_{\perp,\ell} & \geq & 25\,\text{GeV}\,, & \quad & |\eta_\ell| & \leq & 2.5 \\ p_{\perp,j} & \geq & 30\,\text{GeV}\,, & \quad & |\eta_j| & \leq & 5\,, \end{array}$$

where jets are defined by the antik_T algorithm with $R = 0.4$. In addition a cut on the missing transverse momentum has been applied,

$$\not{E}_T \geq 25\,\text{GeV}\,, \tag{1.4}$$

which of course is practically given by the combined neutrino momenta.

In Figure 5 inclusive and exclusive jet multiplicities as obtained from the samples described above are displayed. They clearly show that especially for jet multiplicities $N_{\text{jet}} \geq 1$ the impact of multijet merging is sizable and important. Furthermore, there is a visible difference in the overall rate of about a factor of 2 between the results with and without the Higgs boson. This becomes even more visible when considering cross sections after the application of a jet veto, cf. the right panel of Figure 6. Multijet merging leads to jets that are visibly harder – the LOOP2+PS results fall of very quickly with respect to the merged result, see the left panel of Fig. 5. However, since the bulk of the inclusive cross section is related to jet transverse momenta below about 30 GeV, the jet-vetoed cross section saturates relatively quickly and is thus correspondingly independent of the hard tails in transverse momentum. This ultimately leads to effects of the order of about 10% or so from multijet merging. At the same time, in the linear plot of the jet-vetoed cross section the rate difference due to the inclusion of the Higgs boson becomes visible. As expected, these differences manifest themselves in the usual kinematic regions stemming from spin effects in the decay of the W bosons, illustrated in Figure 7. Clearly, the presence of a Higgs boson pushes the leptons closer in phase space. Since the overall rate is dominated by the 0-jet bin, the differences between merged and LO samples are again relatively small, of the order of 10% or below.

To summarise: the application of multijet merging to loop–induced processes $gg \to VV^{(*)}$ leads to visibly harder jet spectra and significantly larger jet multiplicities, irrespective of whether this process is mediated by a Higgs boson or not. It is clearly the overall scale of the process and the fact that the initial states are identical that is responsible here. The effect on jet-vetoed cross sections in the 0-jet bin is small, 10% or below, since these cross sections essentially appear after integration over the jet-cross section up to the veto scale. Clearly, though, this would be different when asking for exactly one jet and vetoing further jets. The impact of the merging is small on the lepton correlations in the regions, that are important for the definition of signal and background regions.

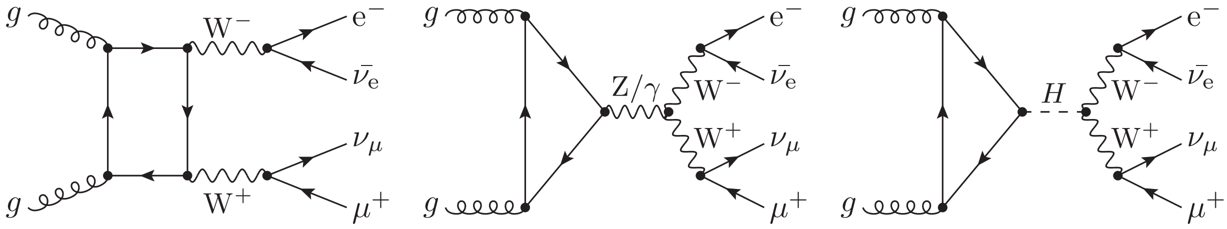

Fig. 3: Leading order Feynman diagrams contributing to $gg \to \ell\bar{\nu}_\ell\bar{\ell}'\nu_{\ell'}$.

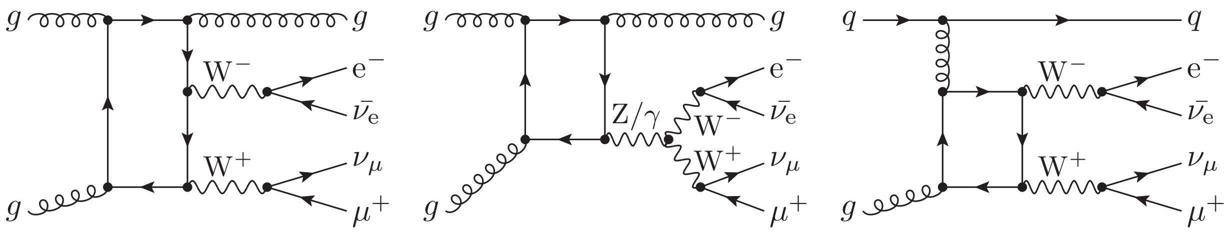

Fig. 4: Leading order Feynman diagrams contributing to the background production of final states $\ell\bar{\nu}_\ell\bar{\ell}'\nu_{\ell'}$+jet through a quark loop.

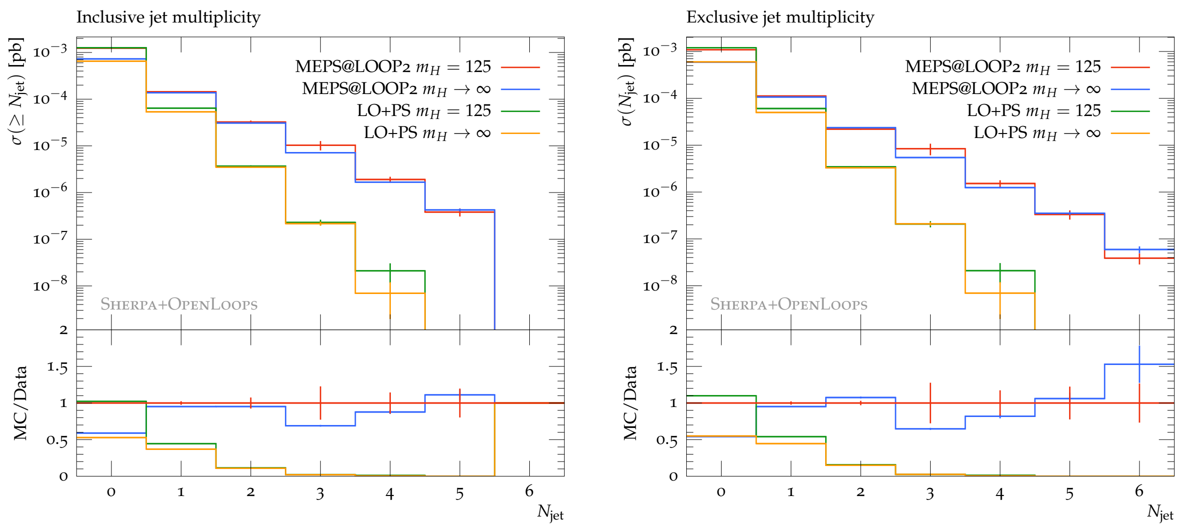

Fig. 5: Inclusive (left) and exclusive (right) jet cross sections with and without multijet merging and with ($m_H = 125$ GeV) and without ($m_H \to \infty$) including a Higgs boson, including multijet merging or merely relying on the parton shower to simulate all QCD emissions.

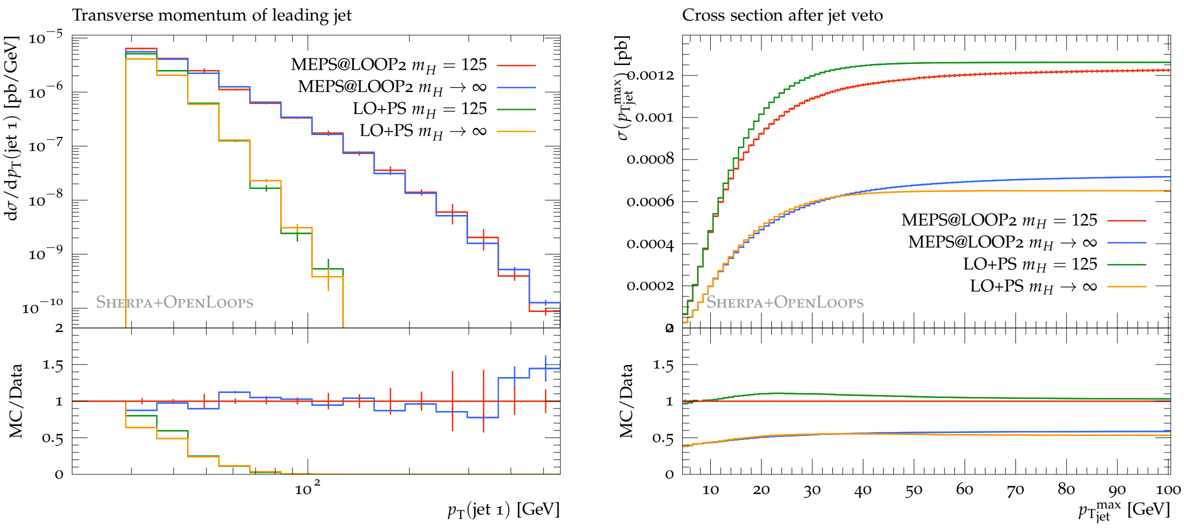

Fig. 6: Differential cross section in dependence of the transverse momentum of the leading jet (left) and the cross section after application of a jet veto in dependence on the transverse momentum cut on jets (right).

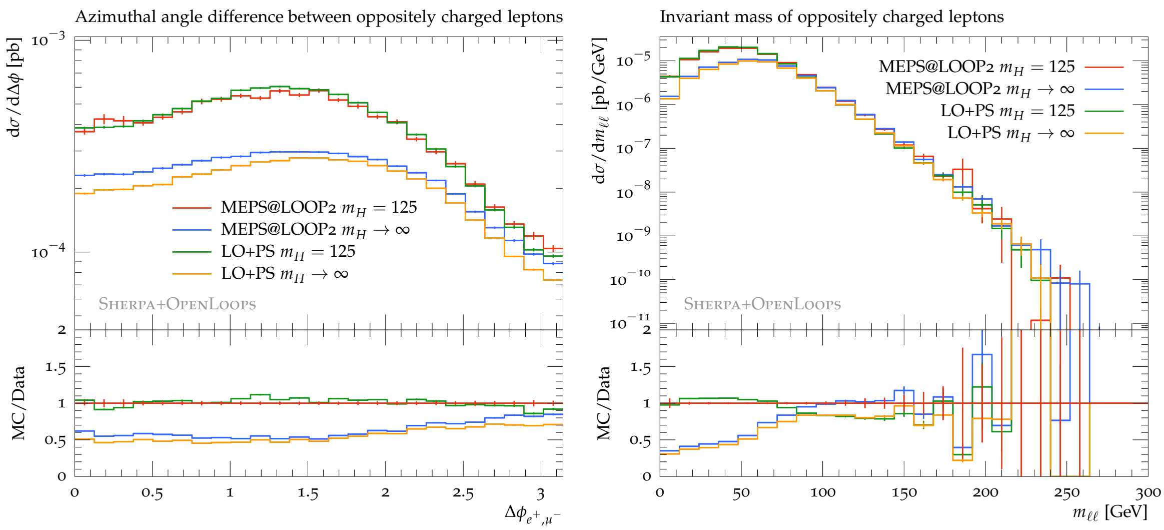

Fig. 7: Differential cross section in dependence on the transverse separation of the two leptons (left) and on their invariant mass (right).

3.3 ATLAS MC comparison for $gg \to H^* \to VV$ and treatment of QCD-related uncertainties

3.4 Higgs boson off-shell simulation with the MCFM and JHU generator frameworks

In the MCFM framework [7], the process $gg \to ZZ$ is simulated at LO in QCD, including the signal $gg \to H \to ZZ$, background $gg \to ZZ$, and their interference. The JHUGen / MELA framework [8–10], provides an extended matrix element library for the anomalous HVV couplings following the formalism

$$A(\mathrm{H}VV) \propto \left[a_1 - e^{i\phi_{\Lambda Q}} \frac{(q_{V1}+q_{V2})^2}{(\Lambda_Q)^2} - e^{i\phi_{\Lambda 1}} \frac{\left(q_{V1}^2+q_{V2}^2\right)}{(\Lambda_1)^2}\right] m_V^2 \epsilon_{V1}^* \epsilon_{V2}^* + a_2 f_{\mu\nu}^{*(1)} f^{*(2),\mu\nu} + a_3 f_{\mu\nu}^{*(1)} \tilde{f}^{*(2),\mu\nu}, \quad (1.5)$$

where $f^{(i)\mu\nu} = \epsilon_{Vi}^{\mu} q_{Vi}^{\nu} - \epsilon_{Vi}^{\nu} q_{Vi}^{\mu}$ is the field strength tensor of a gauge boson with momentum q_{Vi} and polarization vector ϵ_{Vi}, $\tilde{f}_{\mu\nu}^{(i)} = \frac{1}{2}\epsilon_{\mu\nu\rho\sigma} f^{(i),\rho\sigma}$ is the dual field strength tensor. The above q^2 expansion is equivalent to the effective Lagrangian notation with operators up to dimension five

$$\begin{aligned}
L(\mathrm{H}VV) \propto \quad & a_1 \frac{m_Z^2}{2} \mathrm{H} Z^{\mu} Z_{\mu} - \frac{\kappa_1}{(\Lambda_1)^2} m_Z^2 \mathrm{H} Z^{\mu} \Box Z_{\mu} - \frac{\kappa_3}{2\,(\Lambda_Q)^2} m_Z^2 \Box \mathrm{H} Z^{\mu} Z_{\mu} - \frac{1}{2} a_2 \mathrm{H} Z^{\mu\nu} Z_{\mu\nu} - \frac{1}{2} a_3 \mathrm{H} Z^{\mu\nu} \tilde{Z}_{\mu\nu} \\
& + a_1^{\mathrm{WW}} m_{\mathrm{W}}^2 \mathrm{H} \mathrm{W}^{+\mu} \mathrm{W}_{\mu}^{-} - \frac{1}{\left(\Lambda_1^{\mathrm{WW}}\right)^2} m_{\mathrm{W}}^2 \mathrm{H} \left(\kappa_1^{\mathrm{WW}} \mathrm{W}_{\mu}^{-} \Box \mathrm{W}^{+\mu} + \kappa_2^{\mathrm{WW}} \mathrm{W}_{\mu}^{+} \Box \mathrm{W}^{-\mu}\right) \\
& - \frac{\kappa_3^{\mathrm{WW}}}{(\Lambda_Q)^2} m_{\mathrm{W}}^2 \Box \mathrm{H} \mathrm{W}^{+\mu} \mathrm{W}_{\mu}^{-} - a_2^{\mathrm{WW}} \mathrm{H} \mathrm{W}^{+\mu\nu} \mathrm{W}_{\mu\nu}^{-} - a_3^{\mathrm{WW}} \mathrm{H} \mathrm{W}^{+\mu\nu} \tilde{\mathrm{W}}_{\mu\nu}^{-} \\
& + \frac{\kappa_2^{Z\gamma}}{\left(\Lambda_1^{Z\gamma}\right)^2} m_Z^2 \mathrm{H} Z_{\mu} \partial_{\nu} F^{\mu\nu} - a_2^{Z\gamma} \mathrm{H} F^{\mu\nu} Z_{\mu\nu} - a_3^{Z\gamma} \mathrm{H} F^{\mu\nu} \tilde{Z}_{\mu\nu} - \frac{1}{2} a_2^{\gamma\gamma} \mathrm{H} F^{\mu\nu} F_{\mu\nu} - \frac{1}{2} a_3^{\gamma\gamma} \mathrm{H} F^{\mu\nu} \tilde{F}_{\mu\nu} \\
& - \frac{1}{2} a_2^{\mathrm{gg}} \mathrm{H} G_a^{\mu\nu} G_{\mu\nu}^a - \frac{1}{2} a_3^{\mathrm{gg}} \mathrm{H} G_a^{\mu\nu} \tilde{G}_{\mu\nu}^a, \qquad (1.6)
\end{aligned}$$

where $V_{\mu\nu} = \partial_{\mu} V_{\nu} - \partial_{\nu} V_{\mu}$, $G_{\mu\nu}^a = \partial_{\mu} A_{\nu}^a - \partial_{\nu} A_{\mu}^a + g f^{abc} A_{\mu}^b A_{\nu}^c$, $\tilde{V}^{\mu\nu} = 1/2\epsilon^{\mu\nu\alpha\beta} V_{\alpha\beta}$, Z is the Z field, W is the W field, F is the γ field, and G is the g field.

Both on-shell H production and off-shell H^* production are considered. There is no kinematic limit on either q_{Vi}^2 or $(q_{V1}+q_{V2})^2$, other than the energy of the colliding beams and the relevant parton luminosities. Since the scale of validity of the nonrenormalizable higher-dimensional operators is *a priori* unknown, effective cut-off scales $\Lambda_{V1,i}, \Lambda_{V2,i}, \Lambda_{H,i}$ are introduced for each term in Eq. (1.5) with the form factor scaling the anomalous contribution g_i^{BSM} as

$$g_i = g_i^{\mathrm{SM}} \times \delta_{i1} + g_i^{\mathrm{BSM}} \times \frac{\Lambda_{V1,i}^2 \Lambda_{V2,i}^2 \Lambda_{H,i}^2}{(\Lambda_{V1,i}^2 + |q_{V1}^2|)(\Lambda_{V2,i}^2 + |q_{V2}^2|)(\Lambda_{H,i}^2 + |(q_{V1}+q_{V2})^2|)}\,. \qquad (1.7)$$

In Fig. 8, the $m_{4\ell}$ distributions in the off-shell region in the simulation of the $gg \to ZZ \to 4\ell$ process are shown for the anomalous and SM contributions in Eq. (1.5). In all cases, the background $gg \to ZZ$ and its interference with different signal hypotheses $gg \to H \to ZZ$ are included except in the case of the pure background.

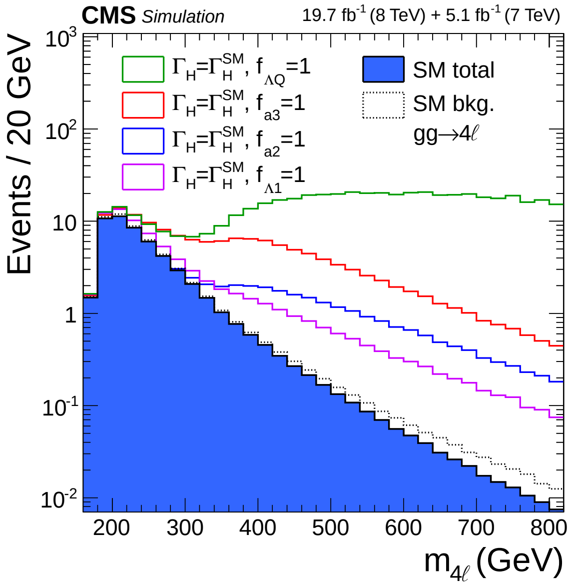

Fig. 8: The $m_{4\ell}$ distributions [11,12] in the off-shell region in the simulation of the $gg \to ZZ \to 4\ell$ process with the Λ_Q, a_3, a_2, and Λ_1 terms, as open histograms, as well as the a_1 term (SM), as the filled histogram, from Eq. (1.5) in decreasing order of enhancement at high mass.

3.5 Interference contributions to gluon-initiated heavy Higgs production in the 2HDM using GoSam

3.5.1 GoSam

GoSam [13, 14] is a package for the automated calculation of one-loop (and tree-level) amplitudes. It can be used either in standalone mode or as a *One Loop Provider* (OLP) in combination with a Monte Carlo program, where the interface is automated, based on the standards defined in Refs. [15, 16]. GoSam is not a library of pre-computed processes, but calculates the amplitude for the process specified by the user in a *run card* on the fly. In the OLP version, the information for the code generation is taken from the order file generated by the Monte Carlo program. The amplitudes are evaluated using D-dimensional reduction at integrand level [17–19], which is available through the reduction procedures and libraries Samurai [20, 21] or Ninja [22, 23]. Alternatively, tensorial reconstruction [24] is also available, based on the library `golem95C` [25–27]. The scalar master integrals can be taken from OneLOop [28] or QcdLoop [29].

The GoSam package comes with the built-in model files `sm`, `smdiag`, `smehc`, `sm_complex`, `smdiag_complex`, where the latter two should be used if complex masses and couplings are present in the amplitude. Complex masses, stemming from the consistent inclusion of decay widths for unstable particles at NLO [30], are particularly important for the inclusion of electroweak corrections, which also can be calculated with GoSam [31]. The model files `smehc` contain the effective Higgs-gluon couplings. It has been used for example in the calculation of the NLO corrections to H+3 jet production in gluon fusion [32, 33] and in the calculation of HH+2 jet production in both the gluon fusion and the vector boson fusion channel [34].

Other models can be imported easily, using the `UFO` (Universal FeynRules Output) [35, 36] format. This feature has been exploited for example in Refs. [37, 38].

Therefore, GoSam comprises all the features which are needed to calculate interference effects, both within and beyond the Standard Model. An example for interference effects within the 2-Higgs-Doublet Model will be given below.

3.5.2 Interference contributions to gluon-initiated heavy Higgs production in the 2HDM

In this section we discuss the loop-induced processes $gg \to ZZ$ and $gg \to VV(\to e^+e^-\mu^+\mu^-/e^+e^-\nu_l\bar{\nu}_l)$ at LO QCD in the context of a CP-conserving Two-Higgs-Doublet-Model (2HDM). In particular, we study the effect of the interference between light and heavy Higgs bosons, and with the background. The 2HDM contains two Higgs doublets, which we name H_1 and H_2. The models can be classified into type I and type II, if we demand no tree-level flavor-changing neutral currents and CP conservation. By convention [39], the up-type quarks couple to H_2. In models of type I, the down-type quarks also couple to H_2, while in type II models, they couple to H_1. The coupling to the leptons can either be through H_1 or H_2, but as our studies are not sensitive to the coupling of the Higgs bosons to leptons, we do not need a further type distinction. The two Higgs doublets form one CP-odd field A and two CP-even Higgs fields h and H due to CP conservation, as well as two charged Higgs bosons $H^{\pm}$. The 2HDM can be described in different basis representations. We make use of the "physical basis", in which the masses of all physical Higgs bosons, the ratio of the vacuum expectation values $\tan\beta := \tan\beta = v_2/v_1$ and the Higgs mixing angle in the CP-even sector α, or alternatively $s_{\beta-\alpha} := \sin(\beta-\alpha)$, are taken as input parameters. We choose $\beta - \alpha$ in between $-\pi/2 \le \beta - \alpha \le \pi/2$, such that $-1 \le s_{\beta-\alpha} \le 1$ and $0 \le c_{\beta-\alpha} \le 1$. Our scenarios are thus specified by the two angles α and β, which completely determine the relative couplings (with respect to the couplings of a SM Higgs boson) of the light and the heavy Higgs boson to quarks and the heavy gauge bosons. They are provided in Eq.(1.8) and Table 1.4 (together with Eq.(1.9) for a decomposition in terms of $\beta - \alpha$ and β). Moreover, our analysis is sensitive to m_h and m_H, whereas it is rather insensitive to the mass of the pseudoscalar m_A and the heavy charged Higgs boson mass $m_{H^\pm}$, as long as they are heavy enough not to open decay modes of the heavy Higgs H into them and as long as the decay mode $H \to hh$ is sub-dominant. The strengths of the Higgs boson couplings to the gauge bosons $V \in \{W, Z\}$ are given by

$$g_V^h = \sin(\beta-\alpha) =: s_{\beta-\alpha}, \qquad g_V^H = \cos(\beta-\alpha) =: c_{\beta-\alpha} \quad . \tag{1.8}$$

The pseudoscalar has no lowest-order couplings to a pair of gauge bosons. It can in principle contribute to the considered processes with four fermions in the final state. Because of the suppression of the Yukawa couplings to leptons, however, these contributions are very small, and thus diagrams involving the pseudoscalar are not of relevance for our discussion. In case of $|s_{\beta-\alpha}| = 1$ the light Higgs boson h couples to the gauge bosons with same strength as the SM Higgs boson. In contrast the coupling of the heavy Higgs boson g_V^H vanishes according to the sum rule $(g_V^h)^2 + (g_V^H)^2 = 1$. Of large relevance for our discussion are the relative couplings of the heavy Higgs boson to bottom-quarks and top-quarks, which are given by

$$\begin{aligned} g_t^H &= \frac{\sin\alpha}{\sin\beta} = -s_{\beta-\alpha}\frac{1}{\tan\beta} + c_{\beta-\alpha}, \\ \text{Type I: } g_b^H &= \frac{\sin\alpha}{\sin\beta} = -s_{\beta-\alpha}\frac{1}{\tan\beta} + c_{\beta-\alpha}, \quad \text{Type II: } g_b^H = \frac{\cos\alpha}{\cos\beta} = s_{\beta-\alpha}\tan\beta + c_{\beta-\alpha} \quad . \end{aligned} \tag{1.9}$$

3.5.2.1 Details of the calculation

We make use of GoSam [13, 14] to discuss the processes $gg \to e^+e^-\mu^+\mu^-$ and $e^+e^-\nu_l\bar{\nu}_l$ (including all three neutrino flavors). For a study of the relevance of interference contributions we also consider the process $gg \to ZZ$, which we generated with the help of `FeynArts` [40] and `FormCalc` [41] and linked to `LoopTools` [41] for the calculation of the employed one-loop Feynman diagrams. We added its amplitudes to a modified version [42] of `vh@nnlo` [43]. It allows to be linked to `2HDMC` [44] which we need for the calculation of the Higgs boson widths Γ_h and Γ_H. In the case of the four lepton final state we have to sum over all possible intermediate configurations leading to the given final state. This particularly means that depending on the sub-process, also intermediate W-bosons as well as non-resonant contributions and photon exchange have to be taken into account. For the numerical integration over the four particle phase space we have combined the GoSam amplitudes with the integration routines provided by `MadEvent` [45, 46].
It is well-known that the calculation of processes including internal Higgs bosons, in particular if one includes higher orders, needs a gauge invariant formulation of the Higgs boson propagator. Since we are working at LO QCD only, a simplistic Breit-Wigner propagator is sufficient for all our purposes. We checked our modified `vh@nnlo` and our GoSam implementations against each other for $gg \to ZZ$ at the amplitude level and reproduced parts of the results presented in Ref. [47] for the four leptonic final state within the numerical uncertainties.
We consider four benchmark scenarios to cover different aspects of a heavy Higgs boson in the phenomenology of a 2HDM, given in Table 1.5. All scenarios include a light Higgs boson with mass $m_h = 125\,\text{GeV}$. We keep the couplings of the light Higgs close to the ones of the SM Higgs by a proper choice of $\tan\beta$ and $s_{\beta-\alpha}$. The masses (and widths) of quarks and gauge bosons are set to $m_t = 172.3\,\text{GeV}, m_b(m_b) = 4.16\,\text{GeV}, m_Z = 91.1876\,\text{GeV}, m_W = 80.398\,\text{GeV}, \Gamma_Z = 2.4952\,\text{GeV}, \Gamma_W = 2.085\,\text{GeV}$.

Our studies presented here are carried out for the LHC with a centre-of-mass energy of $\sqrt{s} = 13\,\text{TeV}$. The role of interference effects is a bit less pronounced at $7/8$ TeV compared to $13\,\text{TeV}$. We make use of `CT10nnlo` [48] as PDF set for the gluon luminosities. Since our calculations are purely performed at LO the renormalization scale dependence enters through the strong coupling α_s only, which we take from the employed PDF set. We choose the renormalization and factorization scale to be dynamical, namely half of the invariant mass of the gauge boson system $\mu_R = \mu_F = m_{VV}/2$, i.e. $\mu_R = \mu_F = m_{4l}/2$ in case of the four leptonic final states. It is known to have a small effect on the cross section [7, 49], which we numerically confirm for the processes under consideration. In case of the four lepton or the two lepton and two neutrino final states, we additionally cut on the transverse momentum and the pseudorapidity of each lepton l, $p_T^l > 10\,\text{GeV}$ and $|\eta_l| < 2.7$, the R-separation between individual leptons $R^{ll'} > 0.1$ as well as $m_{ll} > 5\,\text{GeV}$, where ll is an oppositely charged same-flavour dilepton pair. For the neutrinos we ask for a total missing transverse momentum of $E_T^{\text{miss}} > 70\,\text{GeV}$. The cuts are inspired by the recent ATLAS analysis carried out in Ref. [50]. One of the most important observables is certainly the invariant mass distribution of the four leptons as the two Higgs bosons manifest themselves in Breit-Wigner peaks in this distribution. For the process $gg \to e^+e^-\mu^+\mu^-$ this observable m_{4l} is also experimentally easily accessible due to two electrons and two muons in the final state. In the cases with neutrinos in the final state the situation is more involved. The invariant mass is no longer an observable that is experimentally accessible but only a transverse component can be measured. If one is interested in a heavy Higgs boson that will decay into the four leptons via two intermediate electroweak gauge bosons a sensible choice is to consider the transverse mass of the underlying two boson system. In our case the two boson system can be ZZ as well as WW. We therefore define a general transverse mass via [51]

$$m_{VV,T}^2 = \left(E_{T,ll} + E_{T,\nu\nu}\right)^2 - \left|\vec{p}_{T,ll} + \vec{p}_{T,\nu\nu}\right|^2 \,, \tag{1.10}$$

with

$$E_{T,ll} = \sqrt{p_{ll}^2 + |\vec{p}_{T,ll}|^2}\,, \quad \text{and} \quad E_T^{\text{miss}} = E_{T,\nu\nu} = \left|\vec{p}_{T,\nu\nu}\right| \,. \tag{1.11}$$

3.5.2.2 Discussion of four fermionic final states

We exemplify the results for the four fermionic final state by discussing the results of scenario S1. Figure 9 shows the invariant mass distribution of the four leptons for $gg \to e^+e^-\mu^+\mu^-$ and the transverse mass distribution using the definition in Eq.(1.10) for the processes involving final state neutrinos. We distinguish four different contributions. In red, denoted with 'All', we plot all contributions that lead to the given final state in the considered scenario. In green, we only plot the contribution from the heavy Higgs boson, whereas in blue we also add the interference of the heavy Higgs boson with the background and the light Higgs boson. The contribution $|h + B|^2$, plotted in black, contains besides the contributions without any Higgs also contributions of the light Higgs as well as the interference contributions of the light Higgs boson with non-Higgs diagrams.
In the invariant mass plot of $gg \to e^+e^-\mu^+\mu^-$, see Figure 9 (a), the two Higgs boson peaks at $m_{4l} = 125$ and $200\,\text{GeV}$ can be clearly seen. Due to the very small width of the heavy Higgs boson there is no distortion of the Breit-Wigner shape visible, and also the impact of the interference contribution to the total height of the peak is rather small. The transverse mass distribution for $gg \to e^+e^-\nu_l\bar{\nu}_l$ shows a quite different pattern. First of all there is no peak from the light Higgs boson. The reason for this are the different cuts compared to the process without neutrinos. The requirement

of $E_T^{\text{miss}} > 70\,\text{GeV}$ excludes this region of phase space. Due to the fact that the four momenta of the neutrinos are experimentally not accessible one sets $E_{T,\nu\nu} = \left|\vec{p}_{T,\nu\nu}\right|$, which ignores the invariant mass of the neutrino system. This removes the sharp peak of the heavy Higgs boson, which is visible in the invariant mass distribution of the muon process. Instead of a distinguished peak one obtains a broad distribution. But also here the contribution of the interference remains small. A second difference compared to the muon process is the occurrence of a small dip at around $m_{VV,T} = 180\,\text{GeV}$ in both signal and background. This specific shape is due to the fact that the total contribution to the process with neutrino final state consists of the sum of two different sub-processes, namely the one with the electron neutrino and the ones with muon- and tau neutrino in the final state. Whereas the first sub-process also has contributions from intermediate W-bosons, this is not the case for the latter sub-processes. The two sub-processes therefore show a different kinematical behavior and the sum of the two contributions leads to the given distribution.
For a more detailed discussion of the other scenarios and different observables we refer to Ref. [52].

3.5.2.3 Relevance of interference contributions

The interference contributions of the heavy Higgs boson with the light Higgs boson and the background are significantly enhanced in two cases: Naturally small couplings involved in the signal process increase the mentioned interferences. This is either of relevance in the decoupling limit of the 2HDM where $s_{\beta-\alpha} \to 1$ and thus the coupling of the heavy Higgs boson to gauge bosons vanishes or through a small coupling of the heavy Higgs boson to top- and/or bottom-quarks. According to Eq. (2) the top-quark coupling vanishes for a specific value of $s_{\beta-\alpha}$ for fixed $\tan\beta$. In a 2HDM type I the bottom-quark coupling vanishes for the same value, such that the cross section $\sigma(gg \to H \to VV)$ gets zero, whereas in a 2HDM type II the cross section is minimal. Moreover the interferences are found to be large for an enhanced bottom-quark Yukawa coupling, i.e. large $\tan\beta$. Again, for further details we refer to Ref. [52]. Interferences in the mentioned two cases can help to lift the signal cross section by more than a factor of 2 and thus enhance the sensitivity of heavy Higgs boson searches.

3.5.2.4 Interferences at high invariant masses

So far we focused on the interference effects between the heavy Higgs and the background as well as the heavy Higgs and the light Higgs in the vicinity of the heavy Higgs resonance, since the interference between the light Higgs boson and the background can be considered constant in this region. However, at high invariant masses of the diboson system the interplay between all three contributions h and H and the background B is of relevance, to a certain extent related to the unitarization of the cross section. In Figure 10 we plot the differential cross section $gg \to ZZ$ as a function of the invariant mass of the diboson system m_{ZZ} up to high masses beyond the heavy Higgs resonance. We exemplify the discussion for the three scenarios S2, S3 and S4. The differences between the colored curves display the importance of the different interference terms. Since the figures are obtained for the partonic cross section and we are interested in the relative effects of the interferences among each other, we do not display units for $d\sigma/dm_{ZZ}$. At high invariant masses the interference between the heavy Higgs boson and the background is negligible, in contrast to the interference of the light Higgs and the heavy Higgs boson, which remains large and can have either sign. Moreover the smoothly falling interference of the light Higgs boson and the background comes into the game within a certain window of invariant masses below 1 TeV. Figure 10 depicts different cases, where the interference $h \cdot H$ is either negative similar to the interference $h \cdot B$ or leads to a positive contribution to the differential cross section in a region $m_{ZZ} \in [450\,\text{GeV}, 1000\,\text{GeV}]$. The latter case is true for scenarios S3 or S4, where a sign change of the total depicted contribution leads to a dip and a subsequent "peak"-like structure when added to the background. This structure also appears in the total four particle final state, where the gluon luminosities further suppress the cross section at high invariant masses. Thus all interferences need to be taken into account in order to correctly describe the cross section at high invariant masses.

Table 1.4: Relative couplings g_f^{ϕ} (with respect to the SM coupling) for the two 2HDM types.

Model	g_u^h	g_d^h	g_u^H	g_d^H
Type I	$\cos\alpha/\sin\beta$	$\cos\alpha/\sin\beta$	$\sin\alpha/\sin\beta$	$\sin\alpha/\sin\beta$
Type II	$\cos\alpha/\sin\beta$	$-\sin\alpha/\cos\beta$	$\sin\alpha/\sin\beta$	$\cos\alpha/\cos\beta$

Table 1.5: 2HDM scenarios considered in our analysis.

Scenario	2HDM type	$\tan\beta$	$s_{\beta-\alpha}$	m_H	Γ_H
S1	II	2	-0.995	200 GeV	0.0277 GeV
S2	II	1	0.990	400 GeV	3.605 GeV
S3	I	5	0.950	400 GeV	2.541 GeV
S4	II	20	0.990	400 GeV	5.120 GeV

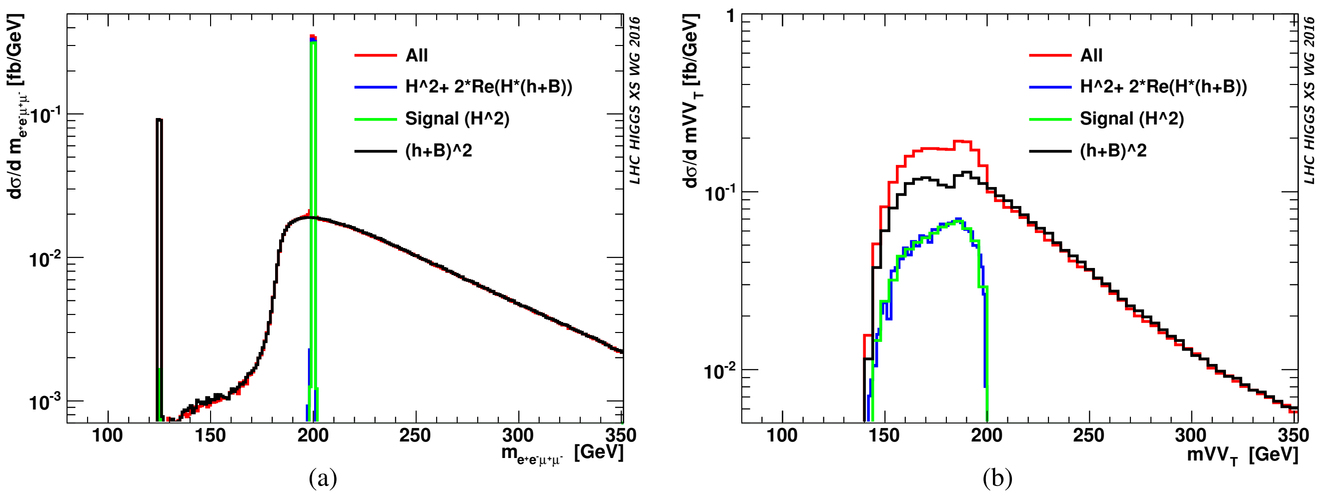

Fig. 9: (a) Invariant mass distribution for $gg \to e^+e^-\mu^+\mu^-$ and (b) transverse mass distribution for $gg \to e^+e^-\nu_l\bar{\nu}_l$ for scenario S1 at $\sqrt{s} = 13\,\text{TeV}$.

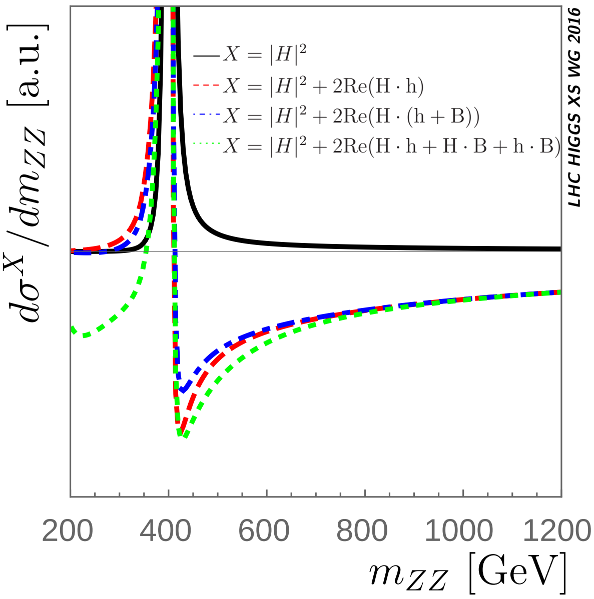

(a)

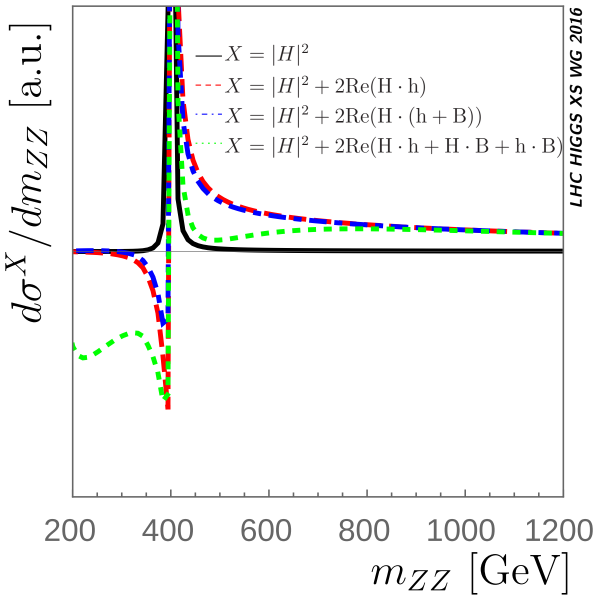

(b)

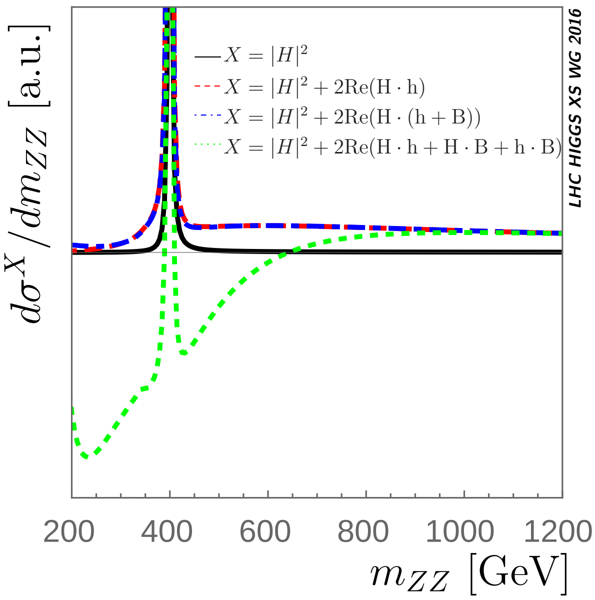

(c)

Fig. 10: Partonic cross sections $d\sigma^X/dm_{zz}$ for $gg \to ZZ$ in arbitrary units as a function of the invariant mass m_{zz} in GeV for scenario (a) S2, (b) S3 and (c) S4 (black: $X = |H|^2$; red, dashed: $X = |H|^2 + 2\mathrm{Re}(H \cdot h)$; blue, dot-dashed: $X = |H|^2 + 2\mathrm{Re}(H \cdot h) + 2\mathrm{Re}(H \cdot B)$; green, dotted: $X = |H|^2 + 2\mathrm{Re}(H \cdot h) + 2\mathrm{Re}(H \cdot B) + 2\mathrm{Re}(h \cdot B)$).

4 $gg \to VV$ at NLO QCD

recommendation for NLO QCD K-factor for gg $(\to H) \to$ VV: 1. continuum background (use K-factor of best available NLO calculation, currently: massless quark loops are included), 2. signal-background interference (use geometric average of signal and continuum background K-factors) (Fabrizio will check how much signal and massless continuum background K-factors diverge at high M_{4l}), show scale uncertainty of massless gg $\to$ VV NLO calculation, discuss **K-factor uncertainty**

4.1 The status of theoretical predictions

A good theoretical control of the off-shell region requires the knowledge of higher order QCD correction for both the signal $pp \to H \to 4l$ and the SM background $pp \to 4l$ processes. At high invariant masses, both the $gg \to H \to 4l$ and the background $gg \to 4l$ processes individually grow with energy, eventually leading to unitarity violations. In the SM, a strong destructive interference between signal and background restores unitarity at high invariant mass, and its proper modeling is important for reliable predictions in the off-shell tail. At invariant masses larger than the top threshold $m_{4l} > 2m_t$ the effect of virtual top quarks running in the loops is non negligible and must be taken into account.

The state of the art for theoretical predictions of signal, background and interference is very different. The signal is known through NLO with exact quark mass dependence [**?**]. NNLO corrections are known as an expansion around the $m_t \to \infty$ limit [], matched to the exact high-energy limit [] to avoid a spurious growth at high energies. **Can we quantify the goodness of this procedure in the high mass region?** Very recently, the N^{3}LO corrections became available [] in the infinite top mass approximation. They turned out to be moderate, with a best stability of the perturbative expansion reached for central scale $\mu = m_H/2$. So far, results are known as an expansion around threshold, which is expected to reproduce the exact result to better than a percent.

We now briefly discuss the status of theoretical description of the background. In the SM, four-lepton production is dominated by quark fusion processes $q\bar{q} \to VV \to 4l$. Recently, NNLO QCD corrections were computed for both the ZZ [] and the WW [] processes, leading to a theoretical uncertainty coming from scale variation of a few percent. In these prediction, the fomally NNLO gluon fusion channel $gg \to 4l$ enters for the first time, i.e. effectively as a LO process. At the LHC, it is enhanced by the large gluon flux and corresponds to roughly 60%(35%) of the total NNLO corrections to the $ZZ(WW)$ process. Despite being subdominant for $pp \to 4l$ production, the $gg \to 4l$ subchannel is of great importance for off-shell studies. First of all, as we already mentioned there is a strong negative interference between $gg \to 4l$ and $gg \to H \to 4l$. Second, the gluon fusion SM background is harder to separate from the Higgs signal.

Computing NLO corrections to $gg \to 4l$ is highly non trivial as it involves the knowledge of complicated two-loop amplitudes with both external and internal massive particles. Very recently, a first step in this direction was performed and NLO QCD corrections for $gg \to ZZ \to 4l$ process were computed in the case of massless quark running in the loop []. This approximation is expected to hold very well below threshold, $m_{4l} < 2m_t \sim 300$ GeV. As in the Higgs case, finite top quark effects are known as an expansion in $1/m_t$ []. Going beyond that would require computing two-loop amplitudes which are currently beyond our technological reach, so the exact result is not expected in the near future.

4.2 Brief description of the NLO computation for $gg \to 4l$

4.2.1 Massless quark contribution

In this section, we briefly report the main details of the $gg \to ZZ \to 4l$ NLO QCD computation []. Despite being a NLO calculation, it poses significant technical challenges. First, complicated two-loop amplitude are required, see Fig. 11 for a representative sample. These amplitudes were recently computed in [] and []. They include decay of the Z bosons and account for full off-shell effects. For the results in [], the C++ implementation of Ref. [] was used. To ensure the result is stable, the code code compares numerical evaluations obtained with different (double, quadruple and, if required, arbitrary) precision settings until the desired accuracy is obtained. For a typical phase space point, the evaluation of all two-loop amplitudes requires about two seconds.

Second, one-loop real emission amplitudes are required, see Fig. 12. Despite being only one-loop amplitudes, they must be evaluated in degenerate soft/collinear kinematics, so they must be quite stable. For the computation in [], these amplitudes were computed from scratch using a mixture of numerical [] and analytical [] unitarity. As a cross-check, the obtained amplitudes were compared against OpenLoops [] for several different kinematic points. Possible numerical instabilitites are cured by increasing the precision of the computation. The typical evaluation time for a phase space point, summed over color and helicities, is about 0.1 seconds. Also in this case, full decay of the Z particles into leptons and off-shell effects are understood. Note that the latter involve a single-resonant diagrams Fig .12(b) which are not present at the LO (due to the fact that triangle-like diagrams vanish at any loop order both in the massless and in the massive theory because of electroweak gauge invariance []). Arbitrary cuts on the final state leptons (and additional jet) are possible.

In this computation, the top quark contribution is neglected. This approximation is expected to work at the 1% level for the total $gg \to ZZ$ cross-section, but it is not reliable in the high invariant mass regime. The bottom quark contribution is included in the massless approximation (see [] for more details).

4.2.2 *Finite top quark effects*

The effect of finite top quark mass in $gg \to ZZ$ at NLO was investigated in []. Similar to what is done in the Higgs case, the authors performed the computation as an expansion in the $m_t \to \infty$ limit. The first two non trivial terms in the expansion were kept, which allowed for a reliable description of the top quark contribution up to invariant masses of order $m_{4l} \sim 300$ GeV. In this computation, only the total $gg \to ZZ$ cross-section was considered, although this should be enough to have a rough estimate of the size of the mass effects. The result on the NLO corrections, compared to the signal case, are shown in Fig. 13.

Beyond the top threshold $m_{4l} \sim 300$ GeV, the expansion [] alone is no longer reliable. Since the full computation is not available, the expansion could be improved along two directions. In principle, it could be matched against the exact high energy behavior []. While this does not pose any conceptual challenge, the computation of the high energy limit is technically more involved than in the Higgs case and it is presently unknown. A second option would be to rescale by the exact LO and hence consider and expansion for the $K-$factor, for which the $1/m_t$ expansion should be better behaved.

4.3 Results and recommendation for the gg $(\to H) \to VV$ interference K-factor

Results for the signal $gg \to H \to 4l$ and background $gg \to 4l$ K-factors are shown in Fig. 14, both at low $m_{4l} < 300$ GeV invariant mass (where the theoretical prediction is complete) and at high invariant mass (where top quark effects are either not included or included through an expansion).

LO and NLO results are both obtained with NLO PDF. In principle, one could envision using LO PDF (and α_s) for the LO results, and this would in general lead to smaller corrections. However, since PDFs fits are still dominated by DIS data, the LO gluon distribution is almost entirely determined by evolution. The large LO gluon flux hence is driven by the large NLO DIS $K-$factor and it is not reliable. Until LO gluon PDFs are obtained by hadronic data, using the NLO gluon distribution is preferable. In principle, NNLO PDFs could be used as well, since the $gg \to 4l$ process enters at NNLO in the $q\bar{q} \to 4l$ computation. However, here we are mostly interested in interference effects, so for consistency with the Higgs case we use NLO PDFs for NLO signal, $gg \to 4l$ background and interference.

Regarding the scale choice, it is well known that for Higgs production an optimal choice would be $\mu \sim m_H/2$ []. Theoretically, it is justified both by large β considerations in the Hgg form factor and by the fact that the average $p_\perp$ of the Higgs boson is $\sim m_H/2$. Empirically, a much better convergence is observed with this scale choice, and a reduced impact of resummation effects []. For off-shell studies, this translates into choosing as a central scale half of the virtuality of the Higgs boson, i.e. $\mu = m_{4l}/2$. Since most of the above consideration are only based on the color flow of the process, the same applied for the background and interference scale choice. Incidentally, we note that this was also the preferred choice for the NNLO $pp \to WW/ZZ$ computations.

Comment the effect of higher order corrections on the signal, with our scale choice. Because of the same color flow, and the similarity of corrections at NLO, use this to comment on perturbative uncertainties.

At this stage, we are not in position of providing a full NLO theoretical prediction valid in the high invariant mass regime, since we do not know top mass effects at NLO. Soft gluon approximations [] and the expansion [] seem to confirm that signal and background $K-$ factors are very similar. This is expected, since the color structure of signal and background is quite similar. To provide a NLO result for the background, given the amount of information available, two options are possible. First, one can consider only massless corrections on top of the exact LO. Second, one could multiply the full (massive) LO by the massless $K-$factor. The difference between the two predictions is a way to probe somehow the uncertainty due to unknown mass effects. For reference, we also show the results of this procedure in Fig. 15 for the signal case, and compare it with the exact result.

Finally, we discuss the $K-$factor for the interference. In principle, the results in [] could be used to obtain a NLO prediction for the interference, at least in the massless approximation. However, this calculation has not been performed yet. Given the similarity of signal and background $K-$factors, until a better computation is available the interference $K-$factor can be obtained as the geometric average of the signal and background $K-$ factors. For its uncertainty, on top of usual (correlated) scale variation one should add the mass uncertainty for the background, computed as described above.

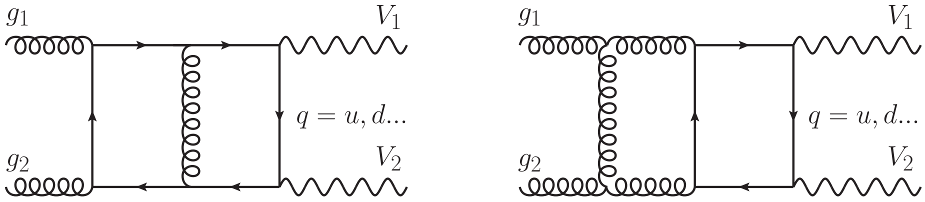

Fig. 11: Representative two-loop diagrams

Fig. 12: Representative double(left) and single(right) resonant one-loop diagrams.

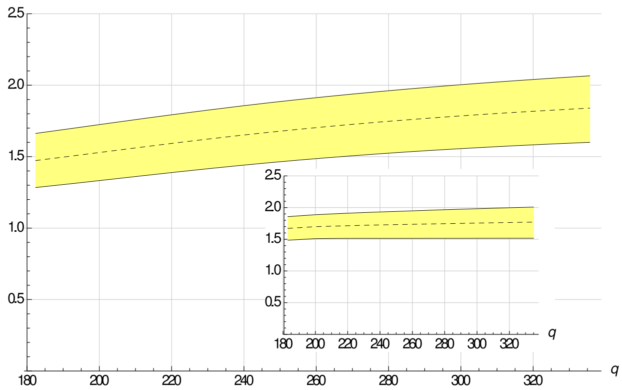

Fig. 13: $K-$factors for signal and background, in the hevay top expansion.

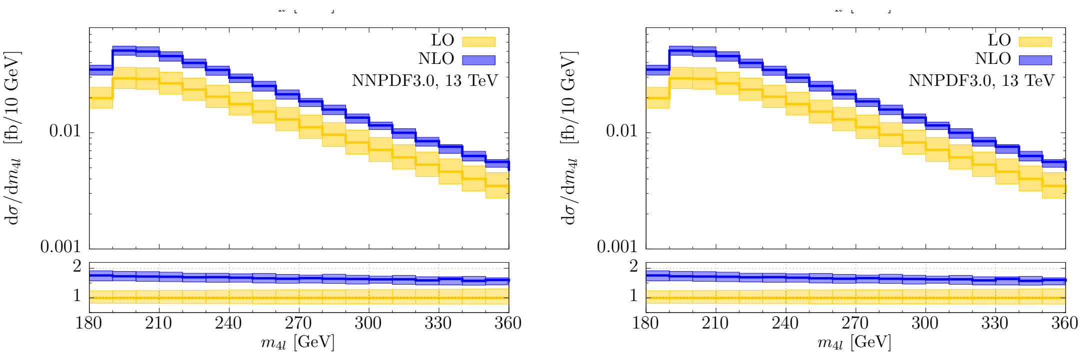

Fig. 14: $K-$factors for signal and background. *figures are just placeholders*

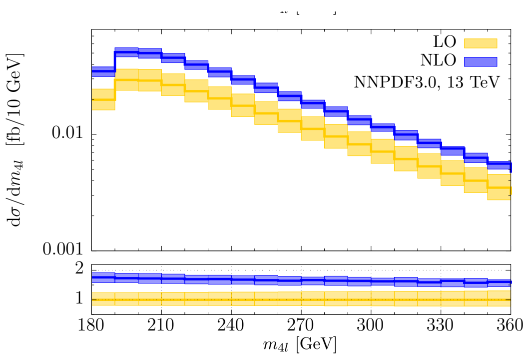

Fig. 15: Comparison of different ways of treating quark mass effects at higher orders

5 $H \to \gamma\gamma$ mode

In this Section we will review the status of the theoretical and experimental treatments of the interference term between the $H \to \gamma\gamma$ and $gg \to \gamma\gamma$.

The natural width of the Higgs boson is an important physics property that could reveal new physics in case of disagreement between the prediction and the measured values. Direct measurements of the Higgs widths are not possible, as the experimental mass resolution is significantly larger than the expected width. The mass resolution of the $\gamma\gamma$ system is about 1.7 GeV for $m_{\gamma\gamma} = 125$ GeV, 400 times larger than the natural width. Measurements of coupling strengths paired with limits on the invisible branching fraction indirectly constrain the width to close to its SM value [53], but this strategy cannot take into account unobserved (but not truly invisible) decay modes.

A new method as introduced by Dixon, Li, and Martin [54, 55], allows to extract an indirect limit on the Higgs width using the interference of the $H \to \gamma\gamma$ signal with respect to the continuum diphoton background ($gg \to \gamma\gamma$ box diagrams). This interference has two parts.

1. An imaginary component reduces the total signal yield by $2-3\%$. Because this effect is degenerate with the coupling (signal strength) measurements, it is only measurable using constraints on the production rates from other channels.
2. The real component is odd around the Higgs boson mass and does not change the yield. However, when folded with the experimental resolution, it engenders a negative shift in the apparent mass.

In the SM, this shift was originally estimated using a simplified resolution model to be approximately 80 MeV [54], and for a width 20 times larger than the SM value, the shift was estimated to approximately 400 MeV.

In this section, we will review the latest developments on theoretical calculations, available MC tools, as well as experimental analyses from ATLAS and CMS collaborations.

5.1 Theory overview

The Higgs boson is dominantly produced by gluon fusion through a top quark loop. Its decay to two photons, $H \to \gamma\gamma$, provides a very clean signature for probing Higgs properties, including its mass. However, there is also a large continuum background to its detection in this channel. It is important to study how much the coherent interference between the Higgs signal and the background could affect distributions in diphoton observables, and possibly use it to constrain Higgs properties.

The interference of the resonant process $ij \to X + H(\to \gamma\gamma)$ with the continuum QCD background $ij \to X + \gamma\gamma$ induced by quark loops can be expressed at the level of the partonic cross section as:

$$\begin{aligned} \delta\hat{\sigma}_{ij\to X+H\to\gamma\gamma} &= -2(\hat{s}-m_H^2)\,\frac{\mathrm{Re}\left(\mathcal{A}_{ij\to X+H}\mathcal{A}_{H\to\gamma\gamma}\mathcal{A}^*_{\mathrm{cont}}\right)}{(\hat{s}-m_H^2)^2+m_H^2\Gamma_H^2} \\ &\quad -2m_H\Gamma_H\,\frac{\mathrm{Im}\left(\mathcal{A}_{ij\to X+H}\mathcal{A}_{H\to\gamma\gamma}\mathcal{A}^*_{\mathrm{cont}}\right)}{(\hat{s}-m_H^2)^2+m_H^2\Gamma_H^2}\,, \end{aligned} \tag{1.12}$$

where m_H and Γ_H are the Higgs mass and decay width, and $\hat{s}$ is the partonic invariant mass. The interference is written in two parts, proportional to the real and imaginary parts of the Higgs Breit-Wigner propagator respectively, to which will be referred to as the real and imaginary part of the interference from now on.

The real part interference is odd in $\hat{s}$ around the Higgs mass peak, and thus its effect on the total $\gamma\gamma$ rate is subdominant as pointed out in ref. [56,57]. The imaginary part of the interference, depending on the phase difference between the signal and background amplitudes, could significantly affect the total cross section. However, for the gluon-gluon partonic subprocess, it was found that the loop-induced background continuum amplitude has a quark mass suppression in its imaginary part for the relevant helicity combinations, making it dominantly real, therefore bearing the same phase as the Higgs production and decay amplitudes [57]. As a result, the contribution of the interference to the total cross section in the gluon fusion channel is highly suppressed at leading order (LO). The main contribution of the interference to the total rate comes from the two-loop imaginary part of the continuum amplitude $gg \to \gamma\gamma$, and only amounts to around 3% of the total signal rate [56].

Later, in ref. [58] it was shown that even though the real part of the interference hardly contributes to the total cross section, it has a quantifiable effect on the position of the diphoton invariant mass peak, producing a shift of $\mathcal{O}(100\,\mathrm{MeV})$ towards a lower mass region, once the smearing effect of the detector was taken into account. In ref. [59], the qg and $q\bar{q}$ channels of this process were studied, completing the full $\mathcal{O}(\alpha_S^2)$ computation of the interference effects between the Higgs diphoton signal and the continuum background at the LHC. Note that the extra qg and $q\bar{q}$ channels involve one QCD emission in the final states, but the corresponding background amplitudes start at tree level, and therefore the relevant interference is of the same order as the LO gg channel in which the background amplitude is induced by a quark loop. The extra LO qg interference is depicted by the top right diagram in fig. 16, and the $q\bar{q}$ channel is related by cross symmetry. It was found that the contribution from the $q\bar{q}$ channel is numerically negligible due to the quark PDF suppression.

More recently, the dominant next-to-leading order (NLO) QCD corrections to the interference were calculated in ref. [54], where the dependence of the mass shift on the acceptance cuts was also studied. The left panel of fig. 17 shows the Gaussian-smeared diphoton invariant mass distribution for the pure signal at both LO and NLO in QCD. Standard acceptance cuts were applied to the photon transverse momenta, $p_{T,\gamma}^{\text{hard/soft}} > 40/30$ GeV, and rapidities, $|\eta_\gamma| < 2.5$. In addition, events were discarded when a jet with $p_{T,j} > 3$ GeV was within $\Delta R_{\gamma j} < 0.4$ of a photon. The scale uncertainty bands were obtained by varying $m_H/2 < \mu_F, \mu_R < 2m_H$ independently. For NLO, an additional qg process was included, where the background is induced by a quark loop as shown in the bottom right diagram of fig. 16; this is required as part of NLO gg channel to cancel the quark to gluon splitting in PDF evolution and reduces dependence on the factorization scale μ_F. As a result, the scale uncertainty bands come mostly from varying the renormalization scale μ_R.

The right panel of fig. 17 shows the corresponding Gaussian-smeared interference contributions. Each band is labelled according to fig. 16. The destructive interference from the imaginary part shows up at two-loop order in the gluon channel in the zero mass limit of light quarks [56]. It produces the offset of the NLO gg curve from zero at $M_{\gamma\gamma} = 125$ GeV.

Figure 18 shows the study of the mass shift dependence on a lower cut on the Higgs transverse momentum $p_T > p_{T,H}$. This strong dependence could potentially be observed experimentally, completely within the $\gamma\gamma$ channel, without having to compare against a mass measurement using the only other high-precision channel, ZZ^{*}[†]. Using only $\gamma\gamma$ events might lead to reduced experimental systematics associated with the absolute photon energy scale. The $p_{T,H}$ dependence of the mass shift was first studied in ref. [55]. The dotted red band includes, in addition, the continuum process $qg \to \gamma\gamma q$ at one loop via a light quark loop, a part of the full $\mathcal{O}(\alpha_s^3)$ correction as explained above. This new contribution partially cancels against the tree-level qg channel, leading to a larger negative Higgs mass shift. The scale variation of the mass shift at finite $p_{T,H}$ is very small, because it is essentially a LO analysis; the scale variation largely cancels in the ratio between interference and signal that enters the mass shift.

Due to large logarithms, the small $p_{T,H}$ portion of fig. 18 is less reliable than the large $p_{T,H}$ portion. In using the $p_{T,H}$ dependence of the mass shift to constrain the Higgs width, the theoretical accuracy will benefit from using a wide first bin in p_T. One could take the difference between apparent Higgs masses for $\gamma\gamma$ events in two bins, those having p_T above and below, say, 40 GeV.

The Higgs width in the SM is $\Gamma_{H,\text{SM}} = 4.07$ MeV, far too narrow to observe directly at the LHC. In global analyses of various Higgs decay channels [61–63], it is impossible to decouple the Higgs width from the couplings in experimental measurements without a further assumption, because the Higgs signal strength is always given by the product of squared couplings for Higgs production and for decay, divided by the Higgs total width Γ_H. Typically, the further assumption is that the Higgs coupling to electroweak vector bosons does not exceed the SM value. However, as was also pointed out in ref. [54], the apparent mass shift could be used to bound the value of the Higgs width. This is because the interference effect has different dependence on the Higgs width, allowing Γ_H to be constrained independently of assumptions about couplings or new decay modes in a lineshape model. Such a measurement would complement more direct measurements of the Higgs width at future colliders such as the ILC [64,65] or a muon collider [66,67], but could be accomplished much earlier.

Using $\mu_{\gamma\gamma}$ to denote the ratio of the experimental signal strength in $gg \to H \to \gamma\gamma$ to the SM prediction ($\sigma/\sigma^{\text{SM}}$), the following equation can be set up,

$$\frac{c_{g\gamma}^2 S}{m_H \Gamma_H} + c_{g\gamma} I = \left(\frac{S}{m_H \Gamma_{H,\text{SM}}} + I \right) \mu_{\gamma\gamma}\,, \tag{1.13}$$

where $c_{g\gamma} = c_g c_\gamma$ is the rescaling factor to be solved to preserve the signal yield when the Higgs width is varied. Once the relation between the $c_{g\gamma}$ and the Higgs width Γ_H is obtained, it can be used to determine the size of the apparent mass shift as a function of Γ_H. Neglecting the interference contribution I to the total rate, and assuming $\mu_{\gamma\gamma} = 1$, the mass shift was found to be proportional to the square root of the Higgs width, $\delta m_H \propto \sqrt{\Gamma_H/\Gamma_{H,\text{SM}}}$, given that the width is much less than the detector resolution. Fig. 19 plots the mass shift with $\mu_{\gamma\gamma} = 1$ and a smearing Gaussian width of 1.7 GeV. It is indeed proportional to $\sqrt{\Gamma_H}$ up to small corrections. If new physics somehow reverses the sign of the Higgs diphoton amplitude, the interference I would be constructive and the mass shift would become positive.

In ref. [68] it was proposed to use another $\gamma\gamma$ sample to determine the Higgs resonance peak, in which the two photons were produced in association with two jets. Although this process is relatively rare, so is the background, making it possible to obtain reasonable statistical uncertainties on the position of the mass peak in this channel despite the lower

[†]The mass shift for ZZ^* is much smaller than for $\gamma\gamma$, as can be inferred from fig. 17 of ref. [60], because $H \to ZZ^*$ is a tree-level decay, while the continuum background $gg \to ZZ^*$ arises at one loop, the same order as $gg \to \gamma\gamma$.

number of events. The production of a Higgs in association with two jets is characteristic of the Vector Boson Fusion (VBF) production mechanism. While, in general terms, VBF is subdominant with respect to GF, it has a very different kinematical signature and can be selected through an appropriate choice of the experimental cuts. From a theoretical point of view, the VBF production mechanism has the additional advantage that perturbative corrections are much smaller than for GF (see e.g. ref. [69]). The effect of the signal-background interference for both the GF and VBF production mechanisms were studied, and the relevant diagrams are given in fig. 20. There are two kinds of backgrounds amplitudes, each of QCD and EW origin. It turns out that the interferences between GF signal and EW background or VBF signal and QCD background are highly suppressed by QCD color factors, and therefore only the remaining combinations are shown in the first two diagrams of fig. 20. In addition, the interference with loop-induced QCD background, as given in the third diagram of fig. 20, was also considered, since it is enhanced by large gluonic luminosity at the LHC.

In fig. 21 the values of the apparent mass shift δm_H obtained for different cuts on the difference in pseudorapidities between the jets $|\Delta\eta_{jj}|$ are shown. The contributions from VBF and GF are presented separately, as well as the total shift. At the bottom of the plot, the total integrated signal is shown, also separated into VBF and GF contributions for the same cuts. For this plot no cut in $p_{T,H}$ was applied, and only events with the invariant mass of the dijet system $M_{jj} > 400$ GeV were considered. When no cut in $|\Delta\eta_{jj}|$ is applied, the shift in the Higgs invariant mass peak position produced by these two main production mechanisms is of the same magnitude, but of opposite sign; hence one observes a partial cancellation between them, with a net shift of around -6 MeV. As the value of $|\Delta\eta_{jj}|_{\text{min}}$ is increased, VBF becomes the dominant contribution, and GF becomes negligible, leading to a shift of around 20 MeV toward lower masses.

Next, the dependence of the mass shift on $p_{T,H}^{\text{min}}$ was studied. In figure 22 the mass shift and the signal cross section for a range of $p_{T,H}^{\text{min}}$ between 0 GeV and 160 GeV is presented. The curves are labelled in the same way as in figure 21. Once again, both production mechanisms contribute to the shift in invariant mass with opposite signs. For this plot, additional cuts in $M_{jj} > 400$ GeV and $|\Delta\eta_{jj}| > 2.8$ were applied, enhancing in this way the VBF contributions. However, at higher $p_{T,H}^{\text{min}}$, GF becomes as important as VBF.

As has already been mentioned, the shift in the Higgs invariant mass peak in $pp \to H(\to \gamma\gamma) + 2\,\text{jets} + X$ is considerably smaller than in the inclusive channel $pp \to H(\to \gamma\gamma) + X$. For appropriate cuts it can be almost zero. This makes it useful as a reference mass for experimental measurement of the mass difference,

$$\Delta m_H^{\gamma\gamma} \equiv \delta m_H^{\gamma\gamma,\,\text{incl}} - \delta m_H^{\gamma\gamma,\,\text{VBF}}\,, \tag{1.14}$$

where $\delta m_H^{\gamma\gamma,\,\text{incl}}$ is the mass shift in the inclusive channel, as computed at NLO in ref. [54], and $\delta m_H^{\gamma\gamma,\,\text{VBF}}$ is the quantity computed in ref. [68]. In computing $\delta m_H^{\gamma\gamma,\,\text{VBF}}$ for use in eq. (1.14) the basic photon and jet p_T and η cuts were imposed, and also $M_{jj} > 400$ GeV, but no additional cuts on $p_{T,H}$ or $\Delta\eta_{jj}$ were applied. This choice of cuts results in a small reference mass shift and a relatively large rate with which to measure it.

The lineshape model of ref. [54], as introduced earlier for the $gg \to \gamma\gamma$ inclusive process, was used in ref. [68] to compute the mass shift for the VBF process. It is in a way relatively independent of the new physics that may increase Γ_H from the SM value. The couplings of the Higgs boson to other SM particles must be modified if the Higgs width is varied, in order to be consistent with the Higgs signal strength measurements already made by the LHC, and prevent the total cross section from suffering large variations. Here, the deviation from SM coupling is described by a rescaling factor $c_{V\gamma} = c_V c_\gamma$, similar to $c_{g\gamma}$ in the $\gamma\gamma$ inclusive case, which is adjusted for different values of Γ_H to maintain the Higgs signal strength near the SM value.

Figure 23 shows how the observable $\Delta m_H^{\gamma\gamma}$ depends on the value of the Higgs width. The dependence is proportional to $\sqrt{\Gamma_H/\Gamma_{H,\text{SM}}}$ to a very good accuracy, as dictated by the linearity of the produced shift in $c_{g\gamma}$ or $c_{V\gamma}$ (in the range shown). It is dominated by the mass shift for the inclusive sample [54]. As was stated before, the main theoretical assumption was that the couplings of the Higgs rescale by real factors, and the same rescaling for the Higgs coupling to gluons as for its coupling to vector boson pairs was assumed; this assumption could easily be relaxed, to the degree allowed by current measurements of the relative yields in different channels. The strong dependence the shift shows on the Higgs width might allow LHC experiments to measure or bound the width.

5.2 Monte Carlo interference implementations

An overview of the Monte Carlo tools available to describe the Higgs lineshape and the signal-background interference is presented in this Section. A first study using these tools is also presented.

5.2.1 Available Tools: Sherpa 2.2.0 with DIRE parton shower

Parton showers have been used for more than three decades to predict the dynamics of multi-particle final states in collider experiments [70, 71]. Recently, a new model was proposed [72], which combines the careful treatment of collinear configurations in parton showers with the correct resummation of soft logarithms in color dipole cascades [73–76]. Following the basic ideas of the dipole formalism, the ordering variable is chosen as the transverse momentum in the soft limit. The evolution equations are based on the parton picture. Color-coherence is implemented by partial fractioning the soft eikonal following the approach in [77], and matching each term to the double logarithmically enhanced part of the DGLAP splitting functions. Enforcing the correct collinear anomalous dimensions then determines all splitting kernels to leading order. Two entirely independent implementations of this model have been provided, which can be used with the two different event generation frameworks Pythia [78] and Sherpa [1, 79].

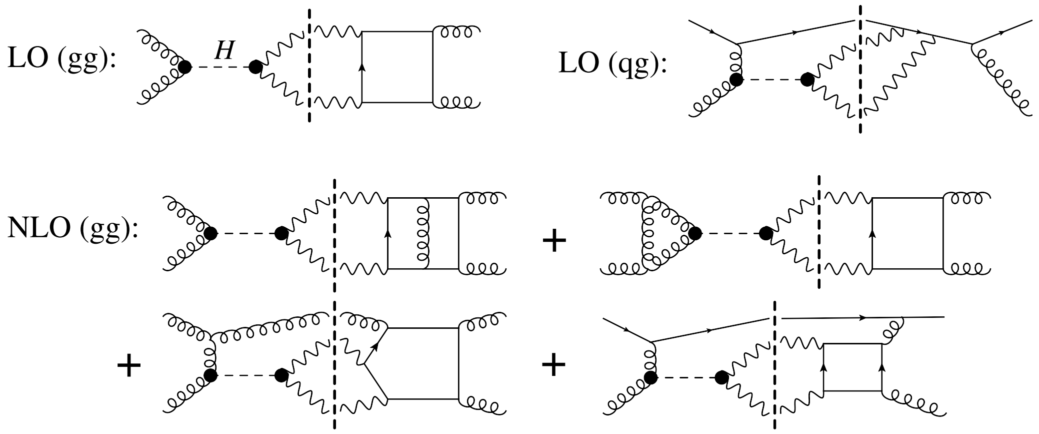

Fig. 16: Representative diagrams for interference between the Higgs resonance and the continuum in the diphoton channel. The dashed vertical lines separate the resonant amplitudes from the continuum ones.

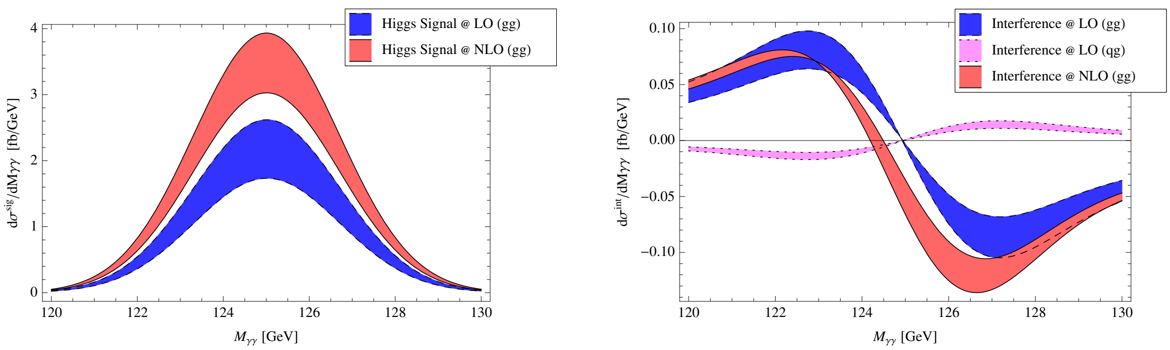

Fig. 17: Diphoton invariant mass $M_{\gamma\gamma}$ distribution for pure signal (left panel) and interference term (right panel) after Gaussian smearing.

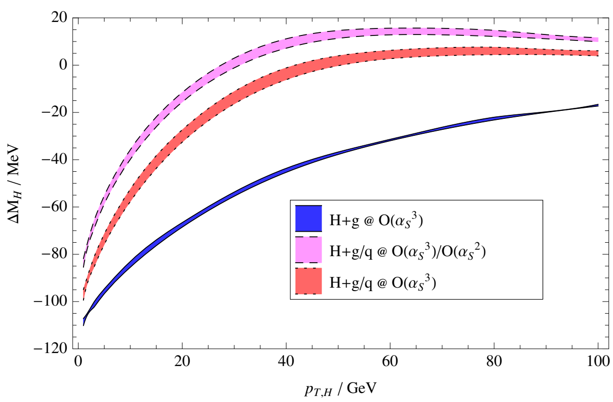

Fig. 18: Apparent mass shift for the SM Higgs boson versus the lower cut on the Higgs transverse momentum, $p_T > p_{T,H}$.

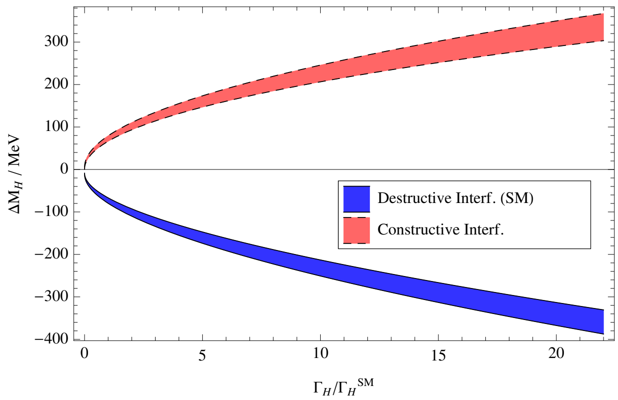

Fig. 19: Higgs mass shift as a function of the Higgs width. The coupling $c_{g\gamma}$ has been adjusted to maintain a constant signal strength, in this case $\mu_{\gamma\gamma} = 1$.

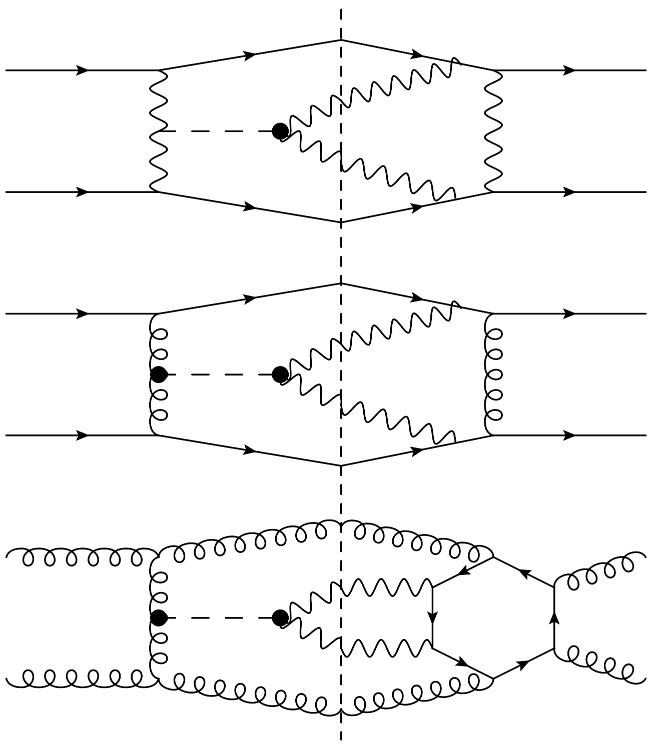

Fig. 20: Examples of the Feynman diagrams computed for the calculation. The vertical dotted line separates signal from background. Above, the VBF signal and EW background con- tributions; in the middle the GF signal with tree level QCD mediated background; below, gluon-initiated signal, with the corresponding loop-induced LO background.

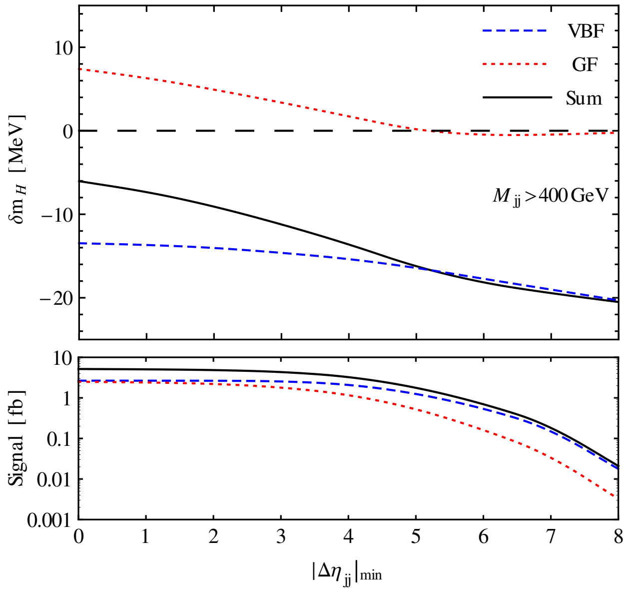

Fig. 21: Top: Plot of mass shift δm_H for different values of $|\Delta\eta_{jj}|_{\text{min}}$. The dashed blue line represents the contribution from the VBF mechanism alone, the dotted red line shows GF only, and the solid black line displays the total shift of the Higgs invariant mass peak. Bottom: Total integrated signal cross section, also separated into VBF and GF contributions for the same cuts. No cut on $p_{T,H}^{\text{min}}$ was applied, and an additional cut was set of $M_{jj} > 400$GeV.

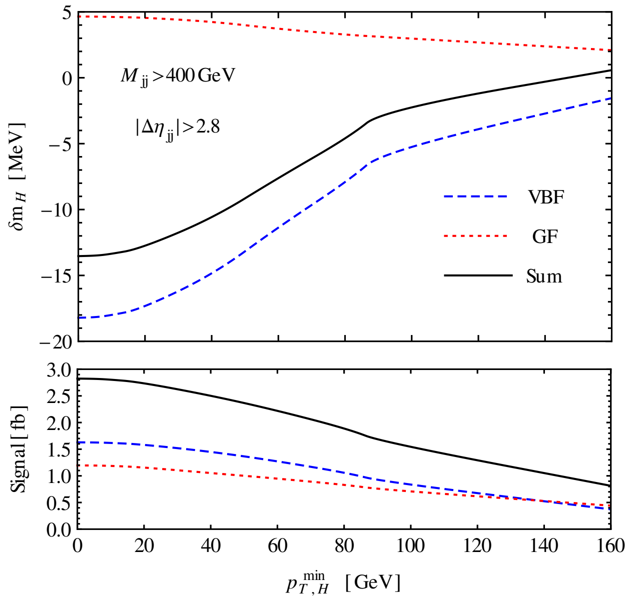

Fig. 22: Top: Plot of mass shift δm_H for different values of $p_{T,H}^{\text{min}}$ for VBF, GF and total contributions. The curves are labelled as in figure 21. Bottom: Total integrated signal, also separated into VBF and GF contributions for the same cuts. The following additional cuts were applied: $M_{jj} > 400$ GeV and $|\Delta\eta_{jj}| > 2.8$.

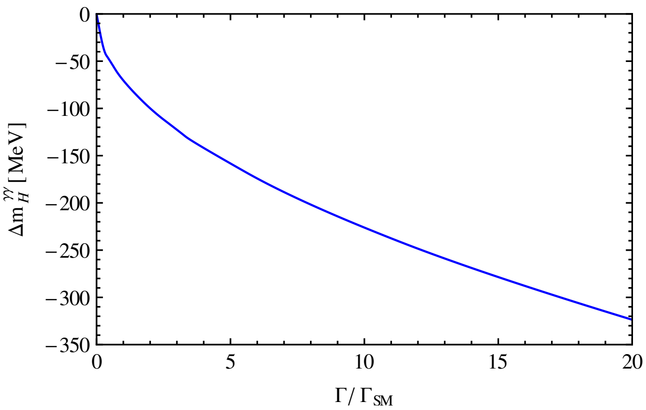

Fig. 23: Plot of measurable mass shift $\Delta m_H^{\gamma\gamma}$ defined in eq. (1.14), as a function of $\Gamma_H/\Gamma_{H,\mathrm{SM}}$.

5.3 Studies from ATLAS

This sections documents the studies by ATLAS collaboration [‡]. Using a more sophisticated resolution model and slightly adjusted selection, as in Ref. [80]. The expected shift in the Higgs boson mass is found to be a bit smaller to about 50 MeV for the SM. Figure 24 shows the mass shift for several width working points. The size of this shift decreases at large transverse momentum of the Higgs boson decay system, which means that the total Higgs boson width is reflected in the difference in the apparent masses between events with low and high p_T^H. A possible analysis strategy to exploit this thus involves splitting the dataset into a low and high p_T^H region, and separately measure the mass difference between these two subsets. A limit of the Higgs width then can be extracted from the measured mass difference.

5.3.1 Feasiblitity studies on Higgs boson width constraint

Ref. [80] carried out a sensitivity study for 300 fb^{-1} of LHC data and 3000 fb^{-1} of HL-LHC data for this strategy. For the HL-LHC data a degradation of the photo identification efficiency was assumed. Photons are selected similar to the analysis of differential cross sections in $H \to \gamma\gamma$ [81]: two isolated photons fulfilling the 'tight' particle identification criterion are selected and required to be within the detector acceptance of $|\eta| < 2.37$; the (sub)leading photon must have $p_T^\gamma > 0.35$ (0.25); the diphoton invariant mass is constructed from these photons. The measurement profits from extremely large systematic uncertainties as most of them, such as the dominant photon energy scale (PES) uncertainty, are correlated between the low and high p_T^H region. These are defined as $p_T^H < 30$ GeV and $p_T^H \geq 30$ GeV. At high-p_T^H the photon tends to be of the order of 10 GeV more-boosted than at low-p_T^H, while the subleading photon is about 10 GeV less boosted. As slightly different photon pT regions are probed, non-linearities in the calorimeter response could in principle introduce some further decorrelation between the systematic uncertainties of both p_T regions. The impact of such a decorrelation on the limit projection is studied, by introduction an additional photon energy scale (PES) uncertainty, with a magnitude of 20% of the total PES systematics. The background modeling uncertainty ('spurious signal') is also taken as fully uncorrelated between the two subsets. The total systematic uncertainty on the mass difference is estimated to be less than 100 MeV, which is significantly smaller than the statistical uncertainty. This analysis will benefit from the high statistics available of the full Run 2 LHC statistics and a HL-LHC.

Next-to-leading order theoretical predictions that account for the interference are used for the mass line shape at nine widths ranging from $1 \times \Gamma_{\rm SM}$ to $1000 \times \Gamma_{\rm SM}$. These predictions are folded with the ATLAS Run I $m_{\gamma\gamma}$ resolution model determined separately for the low- and high-p_T^H samples, to derive the expected shifts in the apparent mass. Figure 25 shows how the mass distribution changes due to the inference for the the low and high-p_T^H regions for the $1 \times \Gamma_{\rm SM}$ and $200 \times \Gamma_{\rm SM}$ after background subtraction. Pseudo-data are then produced by folding a Breit-Wigner of the appropriate width with the resolution model, and then applying the shifts described above. For values of $\Gamma/\Gamma_{\rm SM}$ which lie between the nine widths for which a theoretical prediction is available, the predicted shift due to interference is extrapolated between existing points. The background shapes are taken from Run I data.

These data are used to derive 95% CL upper limits on the Higgs boson width, as shown in Fig. 26. If the Higgs boson has SM width, an expected limit may be set at $220 \times \Gamma_{\rm SM} \approx 880$ MeV with 300 fb^{-1} of data, or $40 \times \Gamma_{\rm SM} \approx 160$ MeV with 3000 fb^{-1}. Introducing an additional uncorrelated PES component to account for unexpected non-linearity effects, reduce the expected sensitivity to $230 \times \Gamma_{\rm SM} \approx 920$ MeV with 300 fb^{-1}. of data, or $50 \times \Gamma_{\rm SM} \approx 200$ MeV with 3000 fb^{-1}. The expected total (statistical) uncertainty on the mass difference assuming a SM width are 420 MeV (410 MeV) for 300 fb^{-1}. and 170 MeV (130 MeV) for 3000 fb^{-1}. The obtained limits may be compared to the current, direct 95% limit from CMS and ATLAS of 1.7 GeV and 2.6 GeV, respectively, using 2011 and 2012 data [82, 83] Reoptimization of the photon identification to maintain the photon/jet discrimination is critical for this statistics-limited analysis. An obvious, but incorrect development of the analysis, would be to use more than two pTH bins. Theoretical uncertainties do not allow for multiple splits below 30 GeV, and above 30 GeV the shift is flat and nearly zero. Below the Higgs peak, the interference produces a simple enhancement in the diphoton spectrum; above the Higgs peak, it produces a deficit. Together, these create an offset between the plateau regions above and below the resonance peak in the $m_{\gamma\gamma}$ spectrum. This is visible in Figure 10. A possible extension to the work presented would be to use not only the shift in the measured peak, but also this offset when evaluating the interference. From the theory side more precise predictions of the interference beyond next-to-leading order and including missing contributions is important. Studies using the SHERPA implementation indicate large sensitivity on the kinematic behaviour of the interference contribution as a function of p_T^H, which need to be further studied and understood prior actual measurements can be carried out.

5.3.2 Impact of interference on Higgs mass measurement

This section intends to document the on-going ATLAS analysis (C. Bescot and L. Fayard) of approving an analysis, aiming to study the expected shift of the Higgs mass in the yy channel due to the interference between $H \to \gamma\gamma$ and $gg \to \gamma\gamma$. This analysis includes two main features, realistic background in the statistical analysis and parton showering. We consider both effects important. The estimated time scale is mid-Jan for ATLAS approval. In Ref. [] the ATLAS

[‡] Contact: F. Bernlochner, C. Bescot, L. Fayard, S. Yuen

collaboration used the existing tools to estimate the impact of the SM interference on the mass measurement Ref. [83]. The mass measurement makes use of extensive categorization to increase the sensitivity on the measured Higgs mass. This is done by dividing the data sets according to 10 criteria, grouping events with similar resolution together. The interference contribution is simulated using SHERPA [] and a tuning of the shower parameters is used such that the signal events approximatively reproduce the p_T distribution of HRes [**?**]. Signal and interference templates are corrected for detector effects using an approximative smearing, which is also employed in the mass measurement to validate the chosen background function. Signal and interference templates are then produced for all 10 categories and injected into an Asimov dataset to extract the expected impact on the mass measurement. The Higgs mass is fitted using the same signal and background shapes as used in Ref. [83]. To properly normalize signal and interference contributions κ-factors are applied. For the interference the signal κ is used due to the lack of a more reliable number. The uncertainties on the choice of the κ-factors, QCD and the shower tuning is assessed by imposing variations and the resulting mass shift assuming the SM width is found to be $XX \pm YY$ MeV. In addition the impact of the shift with widths of 300 and 600 MeV were probed. The induced mass shifts are $XX \pm YY$ MeV and $XX \pm YY$ MeV, respectively. The behaviour of the mass shift evolves linearly with $\sqrt{\Gamma_H}$, as shown by Ref. [54].

5.3.3 Exercise with DIRE parton shower

This sensitivity study follows the basic search strategy exploited in the past by both the CMS and ATLAS experiment for what concerns the $H \rightarrow \gamma\gamma$ [84, 85]. The study is performed only at generator level assuming only gluon fusion production mode (GGH). The parton shower model assumed is the one described in section 5.2.1. Two isolated photons fulfilling loose identification criterion are selected and required to be within the the detector acceptance of $|eta| < 2.5$ and the leading (subleading) photon must have $p_{T1} > 40$ GeV and $p_{T2} > 30$ GeV. The diphoton invariant mass is constructed from these photons and required to be in the $[110 - 150]$ GeV energy range. Figures 27 show the transverse momentum distributions obtained for the two photons after the selection.

Figures 28 show the transverse momentum and the invariant mass of the diphoton system assuming no interference effect.

Finally figures 29 show the diphoton mass shapes for only the interference term and for the signal+ interference.

Different values for the energy resolution can be assumed to fold the generator shapes with a gaussian model. Figure 30 shows the effect of the resolution smearing on the interference term assuming resolution values in the range [1.2-2.2] GeV.

An energy resolution of 1.7 GeV is eventually assumed before comparing the shapes of the pure signal term and of the signal + interference terms in order to evaluate the relative shift introduced by the interference term itself. Figures 31 show this effect. In this case the shift is evaluated fitting the two distribution with a gaussian function and obtained to be equal to $\Delta m = -89$ MeV. The trend of this shift varying the assumption on the value of the energy resolution is also shown in Figure 32. The uncertainties associated to the shifts comes only from the statistical propagation of the errors on the fit parameters.

As outlined in section 5.1 the effect of the shift depends strongly upon the minimum threshold applied on the transverse momentum of the diphoton system. Figure 33 reproduce the results shown in section 5.1 showing that the greater the requirement on the diphoton momentum, the smaller the shift in the mass peak position.

Additional studies are on going in order to evaluate the dependence of the shift upon the natural width of the Higgs.

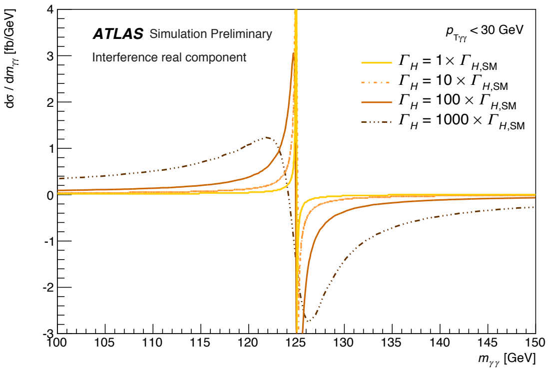

(a) Real Interference

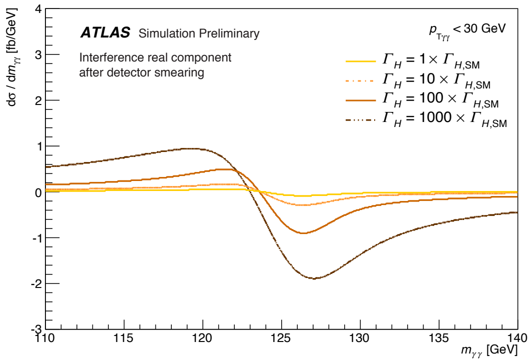

(b) Real term after detector smearing

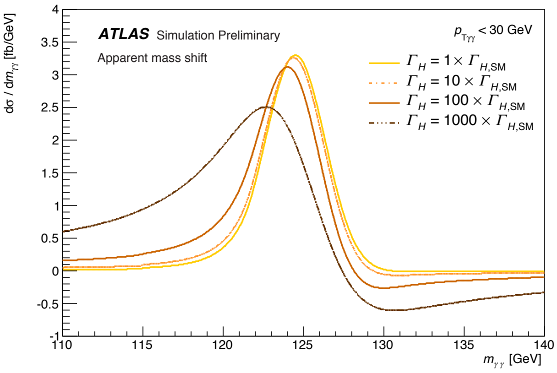

(c) Apparent mass shift

Fig. 24: The real component of the interference (a) is odd around the Higgs boson mass, with a sharp spike but long tails. Smearing this shape with the experimental resolution broadens observed cross section (b), and adding this to the nominal signal model (c) leads to a shift in the apparent mass. The interference and signal line shapes were provided by Dixon and Li, the experimental $m_{\gamma\gamma}$ resolution corresponds to the Run I resolution. **Plots will be updated to conform with YR4 style**

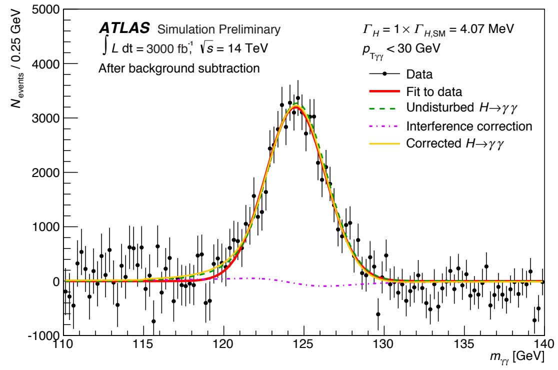

(a) Mass shift for $1 \times \Gamma_{\mathrm{SM}}$ and $p_T^H < 30$ GeV

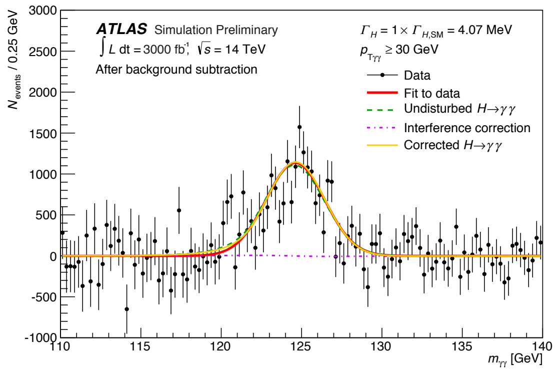

(b) Mass shift for $1 \times \Gamma_{\mathrm{SM}}$ and $p_T^H \geq 30$ GeV

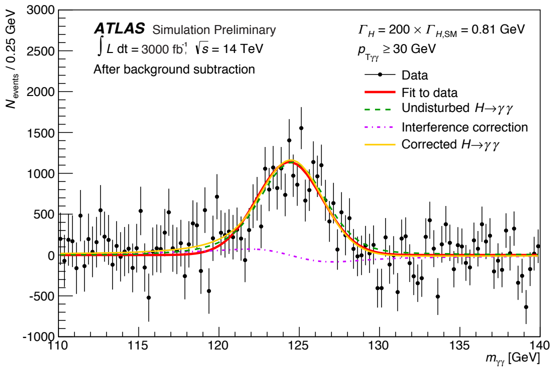

(c) Mass shift for $200 \times \Gamma_{\mathrm{SM}}$ and $p_T^H < 30$ GeV

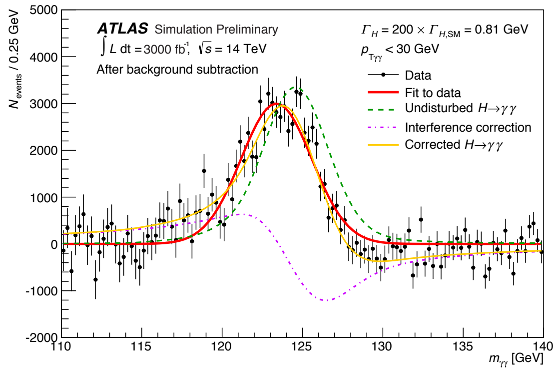

(d) Mass shift for $200 \times \Gamma_{\mathrm{SM}}$ and $p_T^H \geq 30$ GeV

Fig. 25: The mass distributions for the low- and high-p_T^H regions for $1 \times \Gamma_{\mathrm{SM}}$ and $200 \times \Gamma_{\mathrm{SM}}$ after background subtraction are illustrated: the data points correspond to a randomized sample of 3000 fb^{-1}, the green dashed line corresponds to the BW without any interference, the magenta line shows the interference correction, and the solid yellow line the summed signal and interference contribution. The red curve is a fit with a Gaussian signal PDF to illustrate the apparent mass shift. **Plots will be updated to conform with YR4 style**

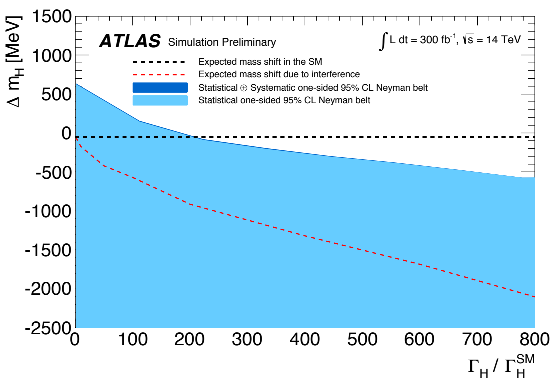

(a) 300 fb^{-1}

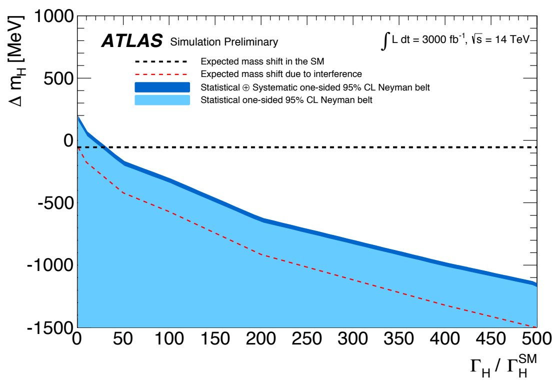

(b) 300 fb^{-1}

Fig. 26: Projected 95% upper limits on the Higgs boson width, at 300 fb^{-1} and 0300 fb^{-1}. The dashed red line depicts the expected shift between the low- and high-p_T samples as a function of the true width. The black dashed line at Δm_H =?54.4 MeV is the expected shift for the SM width. The light/dark shaded region denotes allowed 95% one-sided Neyman confidence belt determined via Asimov data sets taking into account statistical (light) or statistical and systematic (dark) uncertainties. The intercepts between the SM value and the blue curves are the expected upper limits on the width, assuming a SM Higgs boson.

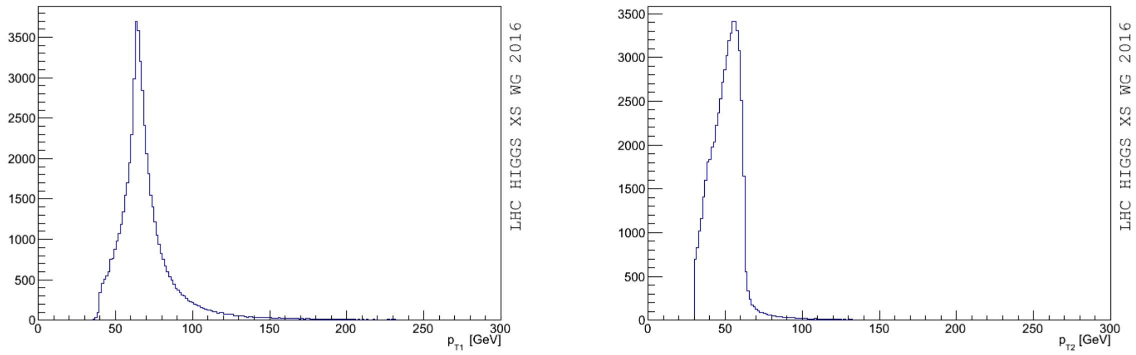

Fig. 27: Transverse momenta of the two photons in the event.

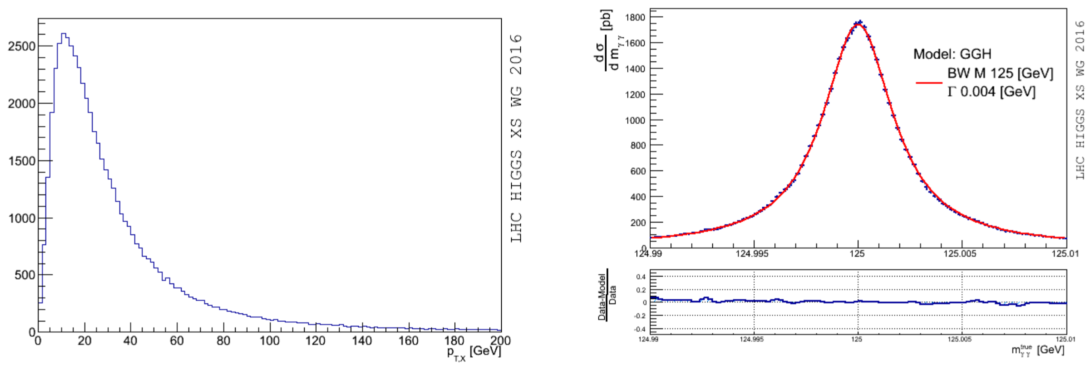

Fig. 28: Diphoton transverse momentum and invariant mass distributions for pure signal term.

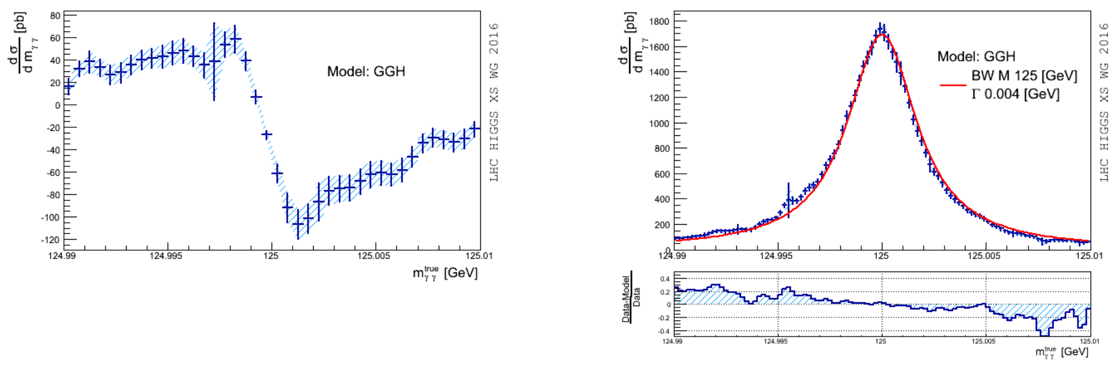

Fig. 29: Pure interference term of the diphoton cross–section on the left and total cross–section (signal+ interference terms) on the right.

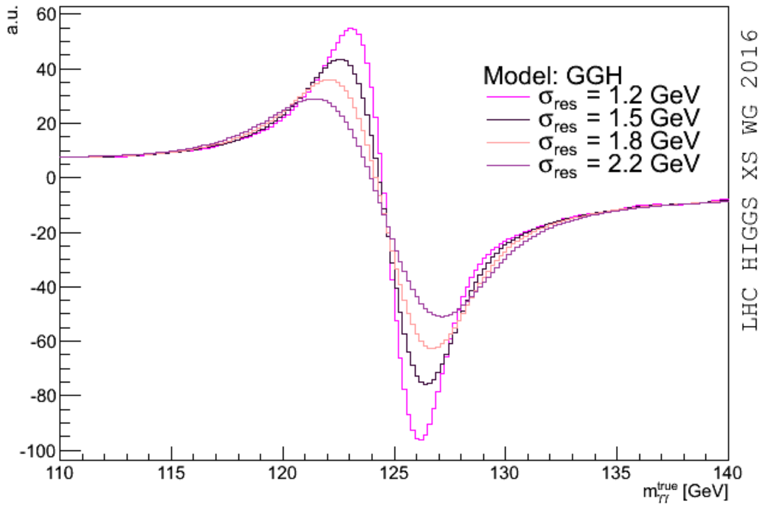

Fig. 30: Interference term assuming different values for the energy smearing resolution.

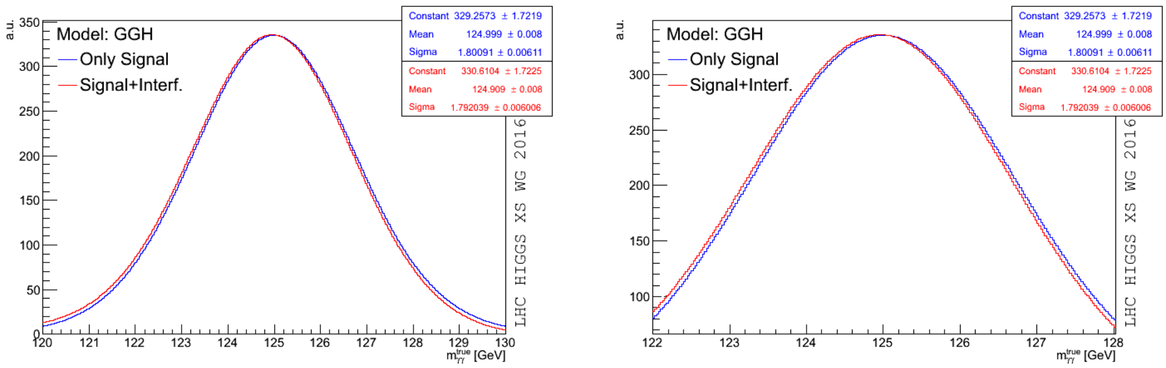

Fig. 31: Pure signal and signal + interference shapes after applying a gaussian energy smearing of 1.7 Gev to simulate detector resolution effects. On the left a zoom around the peak region is applied to better visualize the shift introduced by the interference term.

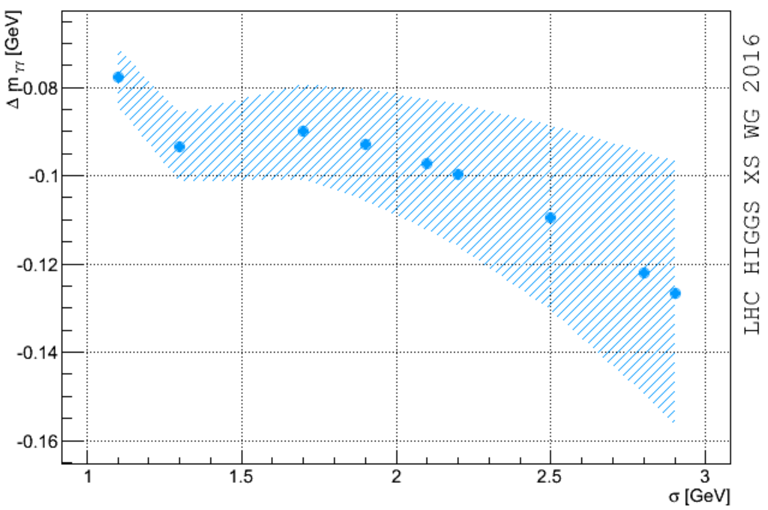

Fig. 32: Shift in the mass peak position as a function of the energy mass resolution assumed.

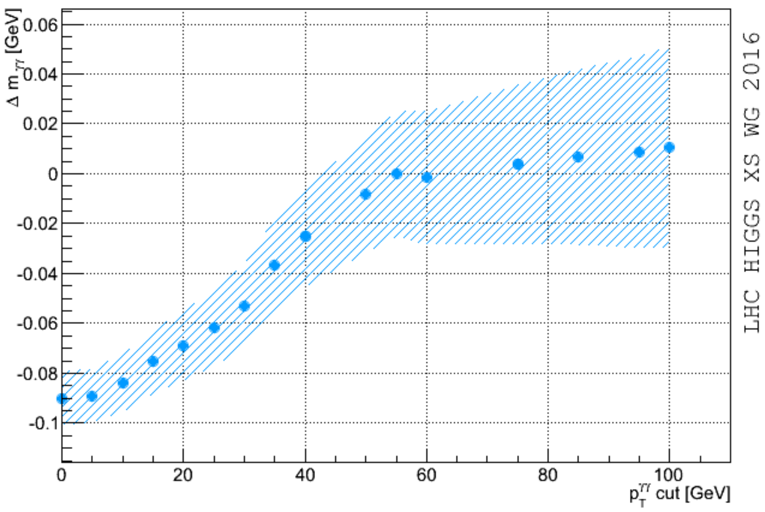

Fig. 33: Shift in the mass peak position as a function of the requirement on the diphoton transverse momentum. The uncertainties associated to the shifts comes only from the statistical propagation of the errors on the fit parameters.

References

[1] T. Gleisberg, S. Höche, F. Krauss, M. Schönherr, S. Schumann, F. Siegert, and J. Winter, *Event generation with Sherpa 1.1*, JHEP **02** (2009) 007, arXiv:0811.4622 [hep-ph]. (8, 25)

[2] S. Catani, F. Krauss, R. Kuhn, and B. R. Webber, *QCD matrix elements + parton showers*, JHEP **11** (2001) 063, hep-ph/0109231. http://www.slac.stanford.edu/spires/find/hep/www?eprint=hep-ph/0109231. (8)

[3] F. Cascioli, P. Maierhofer, and S. Pozzorini, *Scattering Amplitudes with Open Loops*, Phys. Rev. Lett. **108** (2012) 111601, arXiv:1111.5206 [hep-ph]. (8)

[4] A. Denner, S. Dittmaier, and L. Hofer, *COLLIER – A fortran-library for one-loop integrals*, PoS **LL2014** (2014) 071, arXiv:1407.0087 [hep-ph]. (8)

[5] S. Schumann and F. Krauss, *A parton shower algorithm based on Catani-Seymour dipole factorisation*, JHEP **03** (2008) 038, arXiv:0709.1027 [hep-ph]. http://www.slac.stanford.edu/spires/find/hep/www?eprint=arXiv:0709.1027. (8)

[6] F. Cascioli, S. HÃűche, F. Krauss, P. MaierhÃűfer, S. Pozzorini, and F. Siegert, *Precise Higgs-background predictions: merging NLO QCD and squared quark-loop corrections to four-lepton + 0,1 jet production*, JHEP **01** (2014) 046, arXiv:1309.0500 [hep-ph]. (8)

[7] J. M. Campbell, R. K. Ellis, and C. Williams, *Bounding the Higgs width at the LHC using full analytic results for* $gg->e^-e^+\mu^-\mu^+$, JHEP **04** (2014) 060, arXiv:1311.3589 [hep-ph]. (11, 14)

[8] Y. Gao, A. V. Gritsan, Z. Guo, K. Melnikov, M. Schulze, and N. V. Tran, *Spin determination of single-produced resonances at hadron colliders*, Phys. Rev. **D81** (2010) 075022, arXiv:1001.3396 [hep-ph]. (11)

[9] S. Bolognesi, Y. Gao, A. V. Gritsan, K. Melnikov, M. Schulze, N. V. Tran, and A. Whitbeck, *On the spin and parity of a single-produced resonance at the LHC*, Phys. Rev. **D86** (2012) 095031, arXiv:1208.4018 [hep-ph]. (11)

[10] I. Anderson et al., *Constraining anomalous HVV interactions at proton and lepton colliders*, Phys. Rev. **D89** (2014) no. 3, 035007, arXiv:1309.4819 [hep-ph]. (11)

[11] CMS Collaboration, V. Khachatryan et al., *Limits on the Higgs boson lifetime and width from its decay to four charged leptons*, Phys. Rev. **D92** (2015) no. 7, 072010, arXiv:1507.06656 [hep-ex]. (12)

[12] CMS Collaboration, V. Khachatryan et al., *Constraints on the spin-parity and anomalous HVV couplings of the Higgs boson in proton collisions at 7 and 8 TeV*, Phys. Rev. **D92** (2015) no. 1, 012004, arXiv:1411.3441 [hep-ex]. (12)

[13] G. Cullen, N. Greiner, G. Heinrich, G. Luisoni, P. Mastrolia, G. Ossola, T. Reiter, and F. Tramontano, *Automated One-Loop Calculations with GoSam*, Eur. Phys. J. **C72** (2012) 1889, arXiv:1111.2034 [hep-ph]. (13, 14)

[14] G. Cullen et al., *$GOSAM$-2.0: a tool for automated one-loop calculations within the Standard Model and beyond*, Eur. Phys. J. **C74** (2014) no. 8, 3001, arXiv:1404.7096 [hep-ph]. (13, 14)

[15] T. Binoth, F. Boudjema, G. Dissertori, A. Lazopoulos, A. Denner, et al., *A Proposal for a standard interface between Monte Carlo tools and one-loop programs*, Comput.Phys.Commun. **181** (2010) 1612–1622, arXiv:1001.1307 [hep-ph]. (13)

[16] S. Alioli, S. Badger, J. Bellm, B. Biedermann, F. Boudjema, et al., *Update of the Binoth Les Houches Accord for a standard interface between Monte Carlo tools and one-loop programs*, Comput.Phys.Commun. **185** (2014) 560–571, arXiv:1308.3462 [hep-ph]. (13)

[17] G. Ossola, C. G. Papadopoulos, and R. Pittau, *Reducing full one-loop amplitudes to scalar integrals at the integrand level*, Nucl.Phys. **B763** (2007) 147–169, arXiv:hep-ph/0609007 [hep-ph]. (13)

[18] R. Ellis, W. T. Giele, Z. Kunszt, and K. Melnikov, *Masses, fermions and generalized D-dimensional unitarity*, Nucl.Phys. **B822** (2009) 270–282, arXiv:0806.3467 [hep-ph]. (13)

[19] P. Mastrolia, G. Ossola, C. Papadopoulos, and R. Pittau, *Optimizing the Reduction of One-Loop Amplitudes*, JHEP **0806** (2008) 030, arXiv:0803.3964 [hep-ph]. (13)

[20] P. Mastrolia, G. Ossola, T. Reiter, and F. Tramontano, *Scattering AMplitudes from Unitarity-based Reduction Algorithm at the Integrand-level*, JHEP **1008** (2010) 080, arXiv:1006.0710 [hep-ph]. (13)

[21] H. van Deurzen, *Associated Higgs Production at NLO with GoSam*, Acta Phys.Polon. **B44** (2013) no. 11, 2223–2230. (13)

[22] H. van Deurzen, G. Luisoni, P. Mastrolia, E. Mirabella, G. Ossola, and T. Peraro, *Multi-leg One-loop Massive Amplitudes from Integrand Reduction via Laurent Expansion*, JHEP **03** (2014) 115, arXiv:1312.6678 [hep-ph]. (13)

[23] T. Peraro, *Ninja: Automated Integrand Reduction via Laurent Expansion for One-Loop Amplitudes*, Comput. Phys. Commun. **185** (2014) 2771–2797, arXiv:1403.1229 [hep-ph]. (13)

[24] G. Heinrich, G. Ossola, T. Reiter, and F. Tramontano, *Tensorial Reconstruction at the Integrand Level*, JHEP **1010**

(2010) 105, arXiv:1008.2441 [hep-ph]. (13)

[25] T. Binoth, J.-P. Guillet, G. Heinrich, E. Pilon, and T. Reiter, *Golem95: A Numerical program to calculate one-loop tensor integrals with up to six external legs*, Comput.Phys.Commun. **180** (2009) 2317–2330, arXiv:0810.0992 [hep-ph]. (13)

[26] G. Cullen, J. Guillet, G. Heinrich, T. Kleinschmidt, E. Pilon, et al., *Golem95C: A library for one-loop integrals with complex masses*, Comput.Phys.Commun. **182** (2011) 2276–2284, arXiv:1101.5595 [hep-ph]. (13)

[27] J. P. Guillet, G. Heinrich, and J. F. von Soden-Fraunhofen, *Tools for NLO automation: extension of the golem95C integral library*, Comput. Phys. Commun. **185** (2014) 1828–1834, arXiv:1312.3887 [hep-ph]. (13)

[28] A. van Hameren, *OneLOop: For the evaluation of one-loop scalar functions*, Comput.Phys.Commun. **182** (2011) 2427–2438, arXiv:1007.4716 [hep-ph]. (13)

[29] R. K. Ellis and G. Zanderighi, *Scalar one-loop integrals for QCD*, JHEP **02** (2008) 002, arXiv:0712.1851 [hep-ph]. (13)

[30] A. Denner, S. Dittmaier, M. Roth, and L. Wieders, *Electroweak corrections to charged-current $e^+e^- \to 4$ fermion processes: Technical details and further results*, Nucl.Phys. **B724** (2005) 247–294, arXiv:hep-ph/0505042 [hep-ph]. Erratum-ibid. **B854** (2012) 504–507. (13)

[31] M. Chiesa, N. Greiner, and F. Tramontano, *Electroweak corrections for LHC processes*, arXiv:1507.08579 [hep-ph]. (13)

[32] G. Cullen, H. van Deurzen, N. Greiner, G. Luisoni, P. Mastrolia, E. Mirabella, G. Ossola, T. Peraro, and F. Tramontano, *Next-to-Leading-Order QCD Corrections to Higgs Boson Production Plus Three Jets in Gluon Fusion*, Phys. Rev. Lett. **111** (2013) no. 13, 131801, arXiv:1307.4737 [hep-ph]. (13)

[33] N. Greiner, S. Hoeche, G. Luisoni, M. Schonherr, J.-C. Winter, and V. Yundin, *Phenomenological analysis of Higgs boson production through gluon fusion in association with jets*, arXiv:1506.01016 [hep-ph]. (13)

[34] M. J. Dolan, C. Englert, N. Greiner, K. Nordstrom, and M. Spannowsky, *$hhjj$ production at the LHC*, Eur. Phys. J. **C75** (2015) no. 8, 387, arXiv:1506.08008 [hep-ph]. (13)

[35] C. Degrande, C. Duhr, B. Fuks, D. Grellscheid, O. Mattelaer, et al., *UFO - The Universal FeynRules Output*, Comput.Phys.Commun. **183** (2012) 1201–1214, arXiv:1108.2040 [hep-ph]. (13)

[36] C. Degrande, *Automatic evaluation of UV and R2 terms for beyond the Standard Model Lagrangians: a proof-of-principle*, Comput. Phys. Commun. **197** (2015) 239–262, arXiv:1406.3030 [hep-ph]. (13)

[37] N. Greiner, G. Heinrich, J. Reichel, and J. F. von Soden-Fraunhofen, *NLO QCD corrections to diphoton plus jet production through graviton exchange*, JHEP **1311** (2013) 028, arXiv:1308.2194 [hep-ph]. (13)

[38] G. Cullen, N. Greiner, and G. Heinrich, *Susy-QCD corrections to neutralino pair production in association with a jet*, Eur.Phys.J. **C73** (2013) 2388, arXiv:1212.5154 [hep-ph]. (13)

[39] G. Branco, P. Ferreira, L. Lavoura, M. Rebelo, M. Sher, et al., *Theory and phenomenology of two-Higgs-doublet models*, Phys.Rept. **516** (2012) 1–102, arXiv:1106.0034 [hep-ph]. (13)

[40] T. Hahn, *Generating Feynman diagrams and amplitudes with FeynArts 3*, Comput. Phys. Commun. **140** (2001) 418–431, arXiv:hep-ph/0012260 [hep-ph]. (14)

[41] T. Hahn and M. Perez-Victoria, *Automatized one-loop calculations in four and D dimensions*, Comput. Phys. Commun. **118** (1999) 153–165, arXiv:hep-ph/9807565. (14)

[42] R. V. Harlander, S. Liebler, and T. Zirke, *Higgs Strahlung at the Large Hadron Collider in the 2-Higgs-Doublet Model*, JHEP **02** (2014) 023, arXiv:1307.8122 [hep-ph]. (14)

[43] O. Brein, R. V. Harlander, and T. J. E. Zirke, *vh@nnlo - Higgs Strahlung at hadron colliders*, Comput. Phys. Commun. **184** (2013) 998–1003, arXiv:1210.5347 [hep-ph]. (14)

[44] D. Eriksson, J. Rathsman, and O. Stal, *2HDMC: Two-Higgs-Doublet Model Calculator Physics and Manual*, Comput. Phys. Commun. **181** (2010) 189–205, arXiv:0902.0851 [hep-ph]. (14)

[45] F. Maltoni and T. Stelzer, *MadEvent: Automatic event generation with MadGraph*, JHEP **0302** (2003) 027, arXiv:hep-ph/0208156 [hep-ph]. (14)

[46] J. Alwall, P. Demin, S. de Visscher, R. Frederix, M. Herquet, et al., *MadGraph/MadEvent v4: The New Web Generation*, JHEP **0709** (2007) 028, arXiv:0706.2334 [hep-ph]. (14)

[47] N. Kauer and C. OâĂŹBrien, *Heavy Higgs signalâĂŞbackground interference in $gg \to VV$ in the Standard Model plus real singlet*, Eur. Phys. J. **C75** (2015) 374, arXiv:1502.04113 [hep-ph]. (14)

[48] J. Gao, M. Guzzi, J. Huston, H.-L. Lai, Z. Li, P. Nadolsky, J. Pumplin, D. Stump, and C. P. Yuan, *CT10 next-to-next-to-leading order global analysis of QCD*, Phys. Rev. **D89** (2014) no. 3, 033009, arXiv:1302.6246 [hep-ph]. (14)

[49] N. Kauer, *Signal-background interference in gg -> H -> VV*, arXiv:1201.1667 [hep-ph]. [PoSRADCOR2011,027(2011)]. (14)

[50] ATLAS Collaboration, G. Aad et al., *Search for an additional, heavy Higgs boson in the $H \to ZZ$ decay channel at $\sqrt{s}$ = 8 TeV in pp collision data with the ATLAS detector*, arXiv:1507.05930 [hep-ex]. (14)

[51] ATLAS Collaboration, G. Aad et al., *Search for a high-mass Higgs boson decaying to a W boson pair in pp collisions at $\sqrt{s} = 8$ TeV with the ATLAS detector*, arXiv:1509.00389 [hep-ex]. (14)

[52] N. Greiner, S. Liebler, and G. Weiglein, *Interference contributions to gluon initiated heavy Higgs production in the Two-Higgs-Doublet Model*, arXiv:1512.07232 [hep-ph]. (15)

[53] V. Barger, M. Ishida, and W.-Y. Keung, *Total Width of 125 GeV Higgs Boson*, Phys. Rev. Lett. **108** (2012) 261801, arXiv:1203.3456 [hep-ph]. (22)

[54] L. J. Dixon and Y. Li, *Bounding the Higgs Boson Width Through Interferometry*, Phys.Rev.Lett. **111** (2013) 111802, arXiv:1305.3854 [hep-ph]. (22, 23, 24, 31)

[55] S. P. Martin, *Interference of Higgs diphoton signal and background in production with a jet at the LHC*, Phys.Rev. **D88** (2013) no. 1, 013004, arXiv:1303.3342 [hep-ph]. (22, 23)

[56] L. J. Dixon and M. S. Siu, *Resonance continuum interference in the diphoton Higgs signal at the LHC*, Phys.Rev.Lett. **90** (2003) 252001, arXiv:hep-ph/0302233 [hep-ph]. (22, 23)

[57] D. A. Dicus and S. S. Willenbrock, *Photon Pair Production and the Intermediate Mass Higgs Boson*, Phys.Rev. **D37** (1988) 1801. (22)

[58] S. P. Martin, *Shift in the LHC Higgs diphoton mass peak from interference with background*, Phys.Rev. **D86** (2012) 073016, arXiv:1208.1533 [hep-ph]. (22)

[59] D. de Florian, N. Fidanza, R. Hernández-Pinto, J. Mazzitelli, Y. Rotstein Habarnau, and G. Sborlini, *A complete $O(\alpha_S^2)$ calculation of the signal-background interference for the Higgs diphoton decay channel*, Eur.Phys.J. **C73** (2013) 2387, arXiv:1303.1397 [hep-ph]. (22)

[60] N. Kauer and G. Passarino, *Inadequacy of zero-width approximation for a light Higgs boson signal*, JHEP **1208** (2012) 116, arXiv:1206.4803 [hep-ph]. (23)

[61] B. A. Dobrescu and J. D. Lykken, *Coupling spans of the Higgs-like boson*, JHEP **02** (2013) 073, arXiv:1210.3342 [hep-ph]. (23)

[62] A. Djouadi and G. Moreau, *The couplings of the Higgs boson and its CP properties from fits of the signal strengths and their ratios at the 7+8 TeV LHC*, Eur. Phys. J. **C73** (2013) no. 9, 2512, arXiv:1303.6591 [hep-ph]. (23)

[63] CMS Collaboration, *Combination of standard model Higgs boson searches and measurements of the properties of the new boson with a mass near 125 GeV*, . (23)

[64] F. Richard and P. Bambade, *Strategy to measure the Higgs mass, width and invisible decays at ILC*, in *International Linear Colliders (ILC) Workshop Valencia, Spain, November 6-10, 2006*. 2007. arXiv:hep-ph/0703173 [HEP-PH]. (23)

[65] M. E. Peskin, *Comparison of LHC and ILC Capabilities for Higgs Boson Coupling Measurements*, arXiv:1207.2516 [hep-ph]. (23)

[66] T. Han and Z. Liu, *Potential precision of a direct measurement of the Higgs boson total width at a muon collider*, Phys. Rev. **D87** (2013) no. 3, 033007, arXiv:1210.7803 [hep-ph]. (23)

[67] A. Conway and H. Wenzel, *Higgs Measurements at a Muon Collider*, arXiv:1304.5270 [hep-ex]. (23)

[68] F. Coradeschi, D. de Florian, L. J. Dixon, N. Fidanza, S. HÃűche, H. Ita, Y. Li, and J. Mazzitelli, *Interference effects in the $H(\to \gamma\gamma) + 2$ jets channel at the LHC*, Phys. Rev. **D92** (2015) no. 1, 013004, arXiv:1504.05215 [hep-ph]. (23, 24)

[69] P. Bolzoni, F. Maltoni, S.-O. Moch, and M. Zaro, *Higgs production via vector-boson fusion at NNLO in QCD*, Phys. Rev. Lett. **105** (2010) 011801, arXiv:1003.4451 [hep-ph]. (24)

[70] B. R. Webber, *Monte Carlo Simulation of Hard Hadronic Processes*, Ann. Rev. Nucl. Part. Sci. **36** (1986) 253–286. (24)

[71] A. Buckley et al., *General-purpose event generators for LHC physics*, Phys. Rept. **504** (2011) 145–233, arXiv:1101.2599 [hep-ph]. (24)

[72] S. Höche and S. Prestel, *The midpoint between dipole and parton showers*, Eur. Phys. J. **C75** (2015) no. 9, 461, arXiv:1506.05057 [hep-ph]. (24)

[73] G. Gustafson, *Dual Description of a Confined Color Field*, Phys. Lett. **B175** (1986) 453. [,193(1986)]. (24)

[74] G. Gustafson and U. Pettersson, *Dipole Formulation of QCD Cascades*, Nucl. Phys. **B306** (1988) 746. (24)

[75] L. Lönnblad, *ARIADNE version 4: A Program for simulation of QCD cascades implementing the color dipole model*, Comput. Phys. Commun. **71** (1992) 15–31. (24)

[76] H. Kharraziha and L. Lönnblad, *The Linked dipole chain Monte Carlo*, JHEP **03** (1998) 006, arXiv:hep-ph/9709424 [hep-ph]. (24)

[77] S. Catani and M. Seymour, *A General algorithm for calculating jet cross-sections in NLO QCD*, Nucl.Phys. **B485** (1997) 291–419, arXiv:hep-ph/9605323 [hep-ph]. (25)

[78] T. Sjöstrand, S. Ask, J. R. Christiansen, R. Corke, N. Desai, P. Ilten, S. Mrenna, S. Prestel, C. O. Rasmussen, and P. Z. Skands, *An Introduction to PYTHIA 8.2*, Comput. Phys. Commun. **191** (2015) 159–177, arXiv:1410.3012 [hep-ph]. (25)

[79] T. Gleisberg, S. Höche, F. Krauss, A. Schälicke, S. Schumann, and J.-C. Winter, *Sherpa 1. alpha: A Proof of concept version*, JHEP **02** (2004) 056, arXiv:hep-ph/0311263 [hep-ph]. (25)

[80] *Projections for measurements of Higgs boson cross sections, branching ratios and coupling parameters with the ATLAS detector at a HL-LHC*, Tech. Rep. ATL-PHYS-PUB-2013-014, CERN, Geneva, Oct, 2013. https://cds.cern.ch/record/1611186. (30)

[81] ATLAS Collaboration, G. Aad et al., *Measurements of fiducial and differential cross sections for Higgs boson production in the diphoton decay channel at $\sqrt{s} = 8$ TeV with ATLAS*, JHEP **09** (2014) 112, arXiv:1407.4222 [hep-ex]. (30)

[82] CMS Collaboration, V. Khachatryan et al., *Precise determination of the mass of the Higgs boson and tests of compatibility of its couplings with the standard model predictions using proton collisions at 7 and 8 TeV*, Eur.Phys.J. **C75** (2015) no. 5, 212, arXiv:1412.8662 [hep-ex]. (30)

[83] ATLAS Collaboration Collaboration, G. Aad et al., *Measurement of the Higgs boson mass from the $H \to \gamma\gamma$ and $H \to ZZ^* \to 4\ell$ channels with the ATLAS detector using 25 fb^{-1} of pp collision data*, Phys.Rev. **D90** (2014) no. 5, 052004, arXiv:1406.3827 [hep-ex]. (30, 31)

[84] CMS Collaboration, V. Khachatryan et al., *Observation of the diphoton decay of the Higgs boson and measurement of its properties*, Eur. Phys. J. **C74** (2014) no. 10, 3076, arXiv:1407.0558 [hep-ex]. (32)

[85] ATLAS Collaboration, G. Aad et al., *Observation of a new particle in the search for the Standard Model Higgs boson with the ATLAS detector at the LHC*, Phys.Lett. **B716** (2012) 1–29, arXiv:1207.7214 [hep-ex]. (32)